

1 **The new Kr-86 excess ice core proxy for synoptic activity: West Antarctic**
2 **storminess possibly linked to ITCZ movement through the last deglaciation**

3 Christo Buizert¹, Sarah Shackleton², Jeffrey P. Severinghaus², William H. G. Roberts³, Alan Seltzer^{2,4},
4 Bernhard Bereiter⁵, Kenji Kawamura⁶, Daniel Baggenstos⁵, Anaïs J. Orsi^{7,8}, Ikumi Oyabu⁶,
5 Benjamin Birner², Jacob D. Morgan², Edward J. Brook¹, David M. Etheridge^{9,10}, David Thornton^{9,10},
6 Nancy Bertler^{11,12}, Rebecca L. Pyne¹¹, Robert Mulvaney¹³, Ellen Mosley-Thompson¹⁴, Peter D. Neff^{15,16},
7 and Vasilii V. Petrenko¹⁶

Formatted: Superscript

8 ¹College of Earth, Ocean and Atmospheric Sciences, Oregon State University, Corvallis, OR 97331, USA

9 ²Scripps Institution of Oceanography, University of California San Diego, La Jolla, CA 92093, USA

10 ³Geography and Environmental Sciences, Northumbria University, Newcastle, UK and BRIDGE, School
11 of Geographical Sciences, University of Bristol, Bristol, UK

12 ⁴Marine Chemistry and Geochemistry Department, Woods Hole Oceanographic Institution, Woods Hole,
13 MA 02543, USA

14 ⁵Climate and Environmental Physics, Physics Institute, and Oeschger Center for Climate Research,
15 University of Bern, 3012, Bern, Switzerland

16 ⁶National Institute for Polar Research, 10-3 Midori-cho, Tachikawa, Tokyo 190-8518, Japan

17 ⁷Laboratoire des Sciences du Climat et de l'Environnement, LSCE/IPSL, CEA-CNRS-UVSQ, Université
18 Paris-Saclay, l'Orme des merisiers, Gif-sur-Yvette, France

19 ⁸Earth, Ocean and Atmospheric Sciences Department, The University of British Columbia, Vancouver, BC
20 V6T 1Z4, Canada

21 ⁹CSIRO ~~Oceans and Atmosphere~~Environment, PMB 1, Aspendale, Victoria 3195, Australia

22 ¹⁰Australian Antarctic Program Partnership, Institute for Marine & Antarctic Studies, University of
23 Tasmania, Hobart, Tasmania 7004, Australia

24 ¹¹Antarctic Research Centre, Victoria University of Wellington, Wellington, 6012, New Zealand

25 ¹²GNS Science, Lower Hut 5010, New Zealand

26 ¹³British Antarctic Survey, National Environment Research Council, Cambridge CB3 0ET, UK

27 ¹⁴Byrd Polar and Climate Research Center, The Ohio State University, Columbus, OH 43210, USA

28 ¹⁵Department of Soil, Water, and Climate, University of Minnesota, Saint Paul, MN 55108, USA

29 ¹⁶Department of Earth and Environmental Sciences, University of Rochester, Rochester, NY 14627, USA

30

31 *Correspondence to:* Christo Buizert (christo.buizert@oregonstate.edu)

32 **Abstract**

33 Here we present a newly developed ice core gas-phase proxy that directly samples a component of the
34 large-scale atmospheric circulation: synoptic-scale pressure variability. Surface pressure ~~variability~~changes
35 weakly ~~disrupts~~disrupt gravitational isotopic settling in the firn layer, which is recorded in krypton-86
36 excess ($^{86}\text{Kr}_{\text{xs}}$). The $^{86}\text{Kr}_{\text{xs}}$ reflects the time-averaged synoptic pressure variability over several years (site
37 “storminess”), and does not record individual synoptic events. We validate $^{86}\text{Kr}_{\text{xs}}$ using late Holocene ice
38 samples from eleven Antarctic and one Greenland ice core that collectively represent a wide range of
39 surface pressure variability in the modern climate. We find a strong spatial correlation ($r = -0.94, p < 0.01$)
40 between site-average $^{86}\text{Kr}_{\text{xs}}$ and ~~site~~time-averaged synoptic variability from reanalysis data. The main
41 uncertainties in the methodanalysis are the corrections for gas loss and thermal fractionation, and the
42 relatively large scatter in the data. Limited scientific understanding of the firn physics and potential biases
43 of $^{86}\text{Kr}_{\text{xs}}$ require caution in interpreting this proxy at present. We show Antarctic $^{86}\text{Kr}_{\text{xs}}$ is linked to the
44 position of the southern hemisphere eddy-driven subpolar jet (SPJ), with a southern position enhancing
45 pressure variability.

46 We present a $^{86}\text{Kr}_{\text{xs}}$ record covering the last 24 ka from the WAIS Divide ice core. West Antarctic synoptic
47 activity is slightly below modern levels during the last glacial maximum (LGM); increases during the
48 Heinrich Stadial 1 and Younger Dryas North Atlantic cold periods; weakens abruptly at the Holocene onset;
49 remains low during the early and mid-Holocene, and gradually increases to its modern value. The WAIS
50 Divide $^{86}\text{Kr}_{\text{xs}}$ record resembles records of monsoon intensity thought to reflect changes in the meridional
51 position of the intertropical convergence zone (ITCZ) on orbital and millennial timescales, such that West
52 Antarctic storminess is weaker when the ITCZ is displaced northward, and stronger when it is displaced
53 southward. We interpret variations in synoptic activity as reflecting movement of the South Pacific SPJ in
54 parallel to the ITCZ migrations, which is the expected zonal-mean response of the eddy-driven jet in models
55 and proxy data. Past changes to Pacific climate and the El Niño Southern Oscillation (ENSO) may amplify
56 the signal of the SPJ migration. Our interpretation is broadly consistent with opal flux records from the
57 Pacific Antarctic zone thought to reflect wind-driven upwelling.

58 We emphasize that $^{86}\text{Kr}_{\text{xs}}$ is a new proxy, and more work is called for to confirm, replicate and better
59 understand these results; until such time, our conclusions regarding past atmospheric dynamics remain
60 ~~tentative~~speculative. Current scientific understanding of firn air transport and trapping is insufficient to
61 explain all the observed variations in $^{86}\text{Kr}_{\text{xs}}$. A list of suggested future studies is provided.

62 **1 Introduction**

63 **1.1 Motivation and objectives**

64 Proxy records from around the globe show strong evidence for past changes in Earth's atmospheric
65 circulation and hydrological cycle that often far exceed those seen in the relatively short instrumental
66 period.

67 For example, low-latitude records of riverine discharge captured in ocean sediments (Peterson et al., 2000),
68 and isotopic composition of meteoric water captured in dripstone calcite (Cheng et al., 2016), suggest large
69 variations in tropical hydrology and monsoon strength, commonly interpreted as meridional migrations of
70 the intertropical convergence zone or ITCZ (Chiang and Friedman, 2012; Schneider et al., 2014). Such
71 ITCZ movement is seen both in response to insolation changes linked to planetary orbit (Cruz et al., 2005)
72 as well as in response to the abrupt millennial-scale Dansgaard-Oeschger (D-O) and Heinrich cycles of the
73 North-Atlantic (Kanner et al., 2012; Wang et al., 2001); the organizing principle is that the ITCZ follows
74 the thermal equator and therefore migrates towards the warmer (or warming) hemisphere (Broccoli et al.,
75 2006; Chiang and Bitz, 2005).

76 As a second example, the intensity of the El Niño – Southern Oscillation (ENSO), the dominant mode of
77 global interannual climate variability, has changed through time. A variety of proxy data suggest ENSO
78 activity in the 20th century was much stronger than in preceding centuries (Emile-Geay et al., 2015; Fowler
79 et al., 2012; Gergis and Fowler, 2009; Thompson et al., 2013). The vast majority of data and model studies
80 suggest weakened ENSO strength in the mid- and early-Holocene, likely in response to stronger orbitally-
81 driven NH summer insolation at that time (Braconnot et al., 2012; Cane, 2005; Clement et al., 2000; Driscoll
82 et al., 2014; Koutavas et al., 2006; Liu et al., 2000; Liu et al., 2014; Moy et al., 2002; Rein et al., 2005;
83 Tudhope et al., 2001; Zheng et al., 2008); yet other studies suggest there may not be such a clear trend, and
84 simply more variability (Cobb et al., 2013). Intensification of ENSO (or perhaps a more El-Niño-like mean
85 state) may have occurred during the North-Atlantic cold phases of the abrupt D-O and Heinrich cycles
86 (Braconnot et al., 2012; Merkel et al., 2010; Stott et al., 2002; Timmermann et al., 2007). Overall,
87 understanding past and future ENSO variability remains extremely challenging (Cai et al., 2015).

88 As a last example, the strength and meridional position of the southern hemisphere westerlies (SHW) is
89 thought to have changed in the past, which, via Southern Ocean wind-driven upwelling, has potential
90 implications for the global overturning circulation (Marshall and Speer, 2012) and for carbon storage in the
91 abyssal ocean (Anderson et al., 2009; Russell et al., 2006; Toggweiler et al., 2006). The SHW are thought
92 to be shifted equatorward (Kohfeld et al., 2013) during the last glacial maximum (LGM), a shift on which
93 climate models disagree (Rojas et al., 2009; Sime et al., 2013). During the abrupt D-O and Heinrich cycles,
94 the SHW move in parallel with the aforementioned migrations of the ITCZ in both data (Buizert et al.,
95 2018; Marino et al., 2013; Markle et al., 2017) and models (Lee et al., 2011; Pedro et al., 2018; Rind et al.,
96 2001).

97 As these examples clearly illustrate, evidence of past changes to the large-scale atmospheric circulation is
98 widespread. However, proxy evidence of such past changes is typically indirect – for example via isotopes
99 in precipitation, sea surface temperature, ocean frontal positions, windblown dust, or ocean upwelling –
100 complicating their interpretation. Here we present a newly developed noble gas-based ice core proxy, Kr-

101 $^{86}\text{Kr}_{\text{xs}}$), that directly samples a component of the large-scale atmospheric circulation: synoptic-
102 scale pressure variability. Owing to the firm air residence time of several years (Buizert et al., 2013) and the
103 gradual bubble trapping process, each ice core sample contains a distribution of gas ages, rather than a
104 single age. Therefore, $^{86}\text{Kr}_{\text{xs}}$ does not record the passing of individual weather systems, but rather the time-
105 average intensity of synoptic-scale barometric variability.

106 Here we provide the first complete description of this new proxy. We validate and calibrate $^{86}\text{Kr}_{\text{xs}}$ using
107 late-Holocene ice core samples from locations around Antarctica and Greenland that represent a wide range
108 of pressure variability in the modern climate. We discuss the difficulties in using this proxy (analytical
109 precision, surface melt, corrections for sample gas loss and thermal fractionation). Next, we use reanalysis
110 data to better understand the drivers of surface pressure variability in Antarctica. Last, we present an $^{86}\text{Kr}_{\text{xs}}$
111 records from the Antarctic WAIS Divide ice core through the last deglaciation.

112 1.2 Gravitational disequilibrium and Kr-86 excess

113 The upper 50-100 m of the ice sheet accumulation zone consists of firm, the unconsolidated intermediate
114 stage between snow and ice. An interconnected pore network exists within the firm, in which gas transport
115 is dominated by molecular diffusion (Schwander et al., 1993). Diffusion in this stagnant air column results
116 in gravitational enrichment in heavy gas isotopic ratios such as $\delta^{15/14}\text{N-N}_2$, $\delta^{40/36}\text{Ar}$ and $\delta^{86/82}\text{Kr}$ (Schwander,
117 1989; Sowers et al., 1992). In gravitational equilibrium, all these gases attain the same degree of isotopic
118 enrichment per unit mass difference:

$$119 \quad \delta_{\text{grav}}(z) = \left[\exp\left(\frac{\Delta m g z}{RT}\right) - 1 \right] \times 1000\text{‰} \quad (1)$$

120 with Δm the isotopic mass difference ($1 \times 10^{-3} \text{ kg mol}^{-1}$), g the gravitational acceleration, z the depth, R the
121 gas constant and T the Kelvin temperature.

122 Besides molecular diffusion, firm air is mixed and transported via three other processes: downward
123 advection with the sinking ice matrix, convective mixing (used in the firm air literature as an umbrella term
124 to denote vigorous air exchange with the atmosphere via e.g. wind pumping and seasonal convection), and
125 dispersive mixing. These last three transport processes are all driven by large-scale air movement that does
126 not distinguish between isotopologues, and we refer to them collectively as macroscopic air movement. Of
127 particular interest for our proxy is dispersive mixing, which is driven by surface pressure variations. When
128 a low-pressure (high-pressure) system moves into the site, firm air at all depth levels is forced upwards
129 (downwards) to reach hydrostatic equilibrium with the atmosphere – a process called barometric pumping.
130 One can think of the firm layer “breathing” in and out in response to a rising and falling barometer,
131 respectively. Because firm has a finite dispersivity (Schwander et al., 1988), this air movement mixes the
132 interstitial firm air (Buizert and Severinghaus, 2016). The upward air flow due to gradual pore closure is
133 orders of magnitude smaller than the flows driven via barometric pumping, and neglected here.

134 Any type of macroscopic air movement disturbs the gravitational settling, reducing isotopic enrichment
135 below δ_{grav} . Let $\delta^{86}\text{Kr}$, $\delta^{40}\text{Ar}$, and $\delta^{15}\text{N}$ refer to deviations of $^{86}\text{Kr}/^{82}\text{Kr}$, $^{40}\text{Ar}/^{36}\text{Ar}$, and $^{29}\text{N}_2/^{28}\text{N}_2$, respectively,
136 from their ratios in the well-mixed atmosphere. Gases that diffuse faster (such as N_2) will always be closer
137 to gravitational equilibrium than gases that diffuse slower (such as Kr), and in the absence of thermal
138 fractionation $\delta^{86}\text{Kr}/4 < \delta^{40}\text{Ar}/4 < \delta^{15}\text{N} < \delta_{\text{grav}}$. The isotopic differences $\delta^{86}\text{Kr}/4 - \delta^{40}\text{Ar}/4$ and $\delta^{86}\text{Kr}/4 - \delta^{15}\text{N}$

139 thus reflect the degree of gravitational disequilibrium. The magnitudes of the isotopic disequilibria scale in
 140 a predictable way following the molecular diffusion coefficients (Birner et al., 2018); because the diffusion
 141 coefficients of N₂ and Ar are very similar, their disequilibria are comparable in magnitude. We define Kr-
 142 86 excess using the Kr and Ar isotopic difference:

$$143 \quad {}^{86}\text{Kr}_{\text{xs}40} = \frac{\delta^{86}\text{Kr}_{\text{corr}} - \delta^{40}\text{Ar}_{\text{corr}}}{\delta^{40}\text{Ar}_{\text{corr}}} \times 1000 \text{ per meg } \text{‰}^{-1} \quad (2)$$

144 where the “corr” subscript denotes a correction for gas loss (Appendix A1) and thermal fractionation
 145 (Appendix A2). The rationale for including a normalization in the denominator is discussed below. An
 146 alternative Kr-86 excess definition is possible using $\delta^{15}\text{N}$ instead of $\delta^{40}\text{Ar}$:

$$147 \quad {}^{86}\text{Kr}_{\text{xs}15} = \frac{\delta^{86}\text{Kr}_{\text{corr}}/4 - \delta^{15}\text{N}_{\text{corr}}}{\delta^{15}\text{N}_{\text{corr}}} \times 1000 \text{ per meg } \text{‰}^{-1} \quad (3)$$

148 Note that both definitions rely on having measurements of three isotope ratios ($\delta^{86}\text{Kr}$, $\delta^{40}\text{Ar}$ and $\delta^{15}\text{N}$), as
 149 the thermal correction requires $\delta^{40}\text{Ar}$ and $\delta^{15}\text{N}$ be known. The ${}^{86}\text{Kr}_{\text{xs}40}$ definition is preferred, because ~~it~~per
 150 unit mass difference $\delta^{40}\text{Ar}$ is less sensitive to thermal fractionation ~~making~~than $\delta^{15}\text{N}$ is (Grachev and
 151 Severinghaus, 2003a; 2003b); this makes it more suitable for interpreting time series. Unless explicitly
 152 stated otherwise, we use ${}^{86}\text{Kr}_{\text{xs}40}$ as our definition of Kr-86 excess. The ${}^{86}\text{Kr}_{\text{xs}15}$ does provide a way to check
 153 the validity of ${}^{86}\text{Kr}_{\text{xs}40}$ timeseries, and indeed we find good correspondence between both definitions for the
 154 WDC deglacial timeseries (~~Fig-6~~). Because the disequilibrium signal is small, we express ${}^{86}\text{Kr}_{\text{xs}}$ in units
 155 of per meg (parts per million) of gravitational disequilibrium per ‰ of gravitational enrichment. This unit
 156 (per meg ‰⁻¹) is mathematically identical to ‰, but we use it to emphasize the normalization in the
 157 denominator.

158 In the (theoretical) case of full gravitational equilibrium (and no gas loss or thermal fractionation), $\delta^{86}\text{Kr}/4$
 159 = $\delta^{40}\text{Ar}/4 = \delta^{15}\text{N} = \delta_{\text{grav}}$, and therefore ${}^{86}\text{Kr}_{\text{xs}} = 0$. Any type of macroscopic mixing will cause $\delta^{86}\text{Kr}/4 <$
 160 $\delta^{40}\text{Ar}/4 < \delta^{15}\text{N} < \delta_{\text{grav}}$, and thus ${}^{86}\text{Kr}_{\text{xs}} < 0$. In this sense ${}^{86}\text{Kr}_{\text{xs}}$ is a quantitative measure for the degree of
 161 gravitational disequilibrium in the firn layer (Birner et al., 2018; Buizert and Severinghaus, 2016).

162 Kawamura et al. (2013) first describe this gravitational disequilibrium (or kinetic) fractionation effect at
 163 the Megadunes site (Severinghaus et al., 2010), where deep firn cracking leads to a 23 m-thick convective
 164 zone. They suggest that the isotopic disequilibrium can be used to estimate past convective zone thickness.
 165 We show here that sites with small convective zones can nevertheless have very negative ${}^{86}\text{Kr}_{\text{xs}}$, and instead
 166 we suggest that the ice core ${}^{86}\text{Kr}_{\text{xs}}$ is dominated by dispersive mixing driven by barometric pumping from
 167 time-averaged synoptic-scale pressure variability.

168 The principle behind ${}^{86}\text{Kr}_{\text{xs}}$ is illustrated with idealized firn model experiments in Fig. 1. In the absence of
 169 dispersive mixing (Fig. 1A, left panel), all isotope ratios approach δ_{grav} and $\delta^{86}\text{Kr} - \delta^{40}\text{Ar}$ is close to zero –
 170 but not exactly zero owing to downward air advection. Next, we replace a fraction f of the molecular
 171 diffusion with dispersive mixing. With dispersive mixing at $f=0.1$ and $f=0.2$ of total mixing (middle and

172 right panels, respectively), isotopic enrichment is progressively reduced below δ_{grav} (dashed line), making
173 $\delta^{86}\text{Kr} - \delta^{40}\text{Ar}$ (and consequently $^{86}\text{Kr}_{\text{xs}}$) increasingly negative.

174 The ratio of macroscopic over diffusive transport is expressed via the dimensionless Péclet number, given
175 here for advection and dispersion:

$$176 \quad \text{Pe}_X = \frac{w_{\text{air}}L + D_{\text{disp}}}{D_X} \quad (4)$$

177 where Pe_X is the Péclet number for gas X , w_{air} the (downward) advective air velocity, L a characteristic
178 length scale, D_X the diffusion coefficient for gas X , and D_{disp} is the dispersion coefficient (Buizert and
179 Severinghaus, 2016). In agreement with earlier studies (Birner et al., 2018; Kawamura et al., 2013), we find
180 that $\delta^{86}\text{Kr} - \delta^{40}\text{Ar}$ is maximized when molecular and dispersive mixing are equal in magnitude ($f = 0.5$, Fig.
181 1B), corresponding to $\text{Pe}_X \approx 1$. Note that $^{86}\text{Kr}_{\text{xs}}$ responds more linearly to f than $\delta^{86}\text{Kr} - \delta^{40}\text{Ar}$ does, due to
182 $\delta^{40}\text{Ar}$ in the denominator of Eq. (2).

183 In a last idealized experiment, we keep the fraction of dispersion fixed at $f = 0.1$ while we reduce the
184 thickness of the firn column by increasing the site temperature (Fig. 1C). We find that $\delta^{86}\text{Kr} - \delta^{40}\text{Ar}$ scales
185 linearly with firn thickness, here represented by $\delta^{40}\text{Ar}$ on the x-axis. However, $^{86}\text{Kr}_{\text{xs}}$ remains essentially
186 constant due to the normalization by $\delta^{40}\text{Ar}$ in the denominator of Eq. (2). The normalization step is thus
187 necessary to enable meaningful comparison between different sites and time periods that all have different
188 firn thicknesses. For this reason, the definition of $^{86}\text{Kr}_{\text{xs}}$ used here has been updated from the original
189 definition by (Buizert and Severinghaus, 2016).

190 Note that these highly idealized experiments assume dispersive mixing to be a fixed fraction of total
191 transport throughout the firn column, equivalent to a constant Péclet number in the diffusive zone (a
192 convective zone is absent in these simulations). In reality, the Péclet number varies greatly on all spatial
193 scales. On the macroscopic scale (> 1 m), Pe reflects the various transport regimes (Sowers et al., 1992),
194 being highest in the convective and lock-in zones. On the microscopic scale (< 1 cm), hydraulic
195 conductance scales as $\propto r^d$ (with r the pore radius) whereas the diffusive conductance scales as $\propto r^2$. This
196 means that the Darcy flow associated with barometric pumping will concentrate in the widest pores and
197 pathways, leading to a range of effective Péclet numbers within a single sample of firn. At intermediate
198 spatial scales of a few cm, firn density layering introduces strong heterogeneity in transport properties. It is
199 unclear at present whether the competition between diffusive and non-diffusive transport, which occurs at
200 the microscopic pore level, can be accurately represented in macroscopic firn air models via a linear
201 parameterization as is the current practice.

202

203 2 Methods

204 2.1 Ice core sites

205 In this study we use ice samples from eleven ice cores drilled in Antarctica, and one in Greenland. The
206 Antarctic sites are: West Antarctic Ice Sheet (WAIS) Divide core (WDC06A, or WDC), Siple Dome
207 (SDM), James Ross Island (JRI), Bruce Plateau (~~BPBRP~~), Law Dome DE08, Law Dome DE08-OH, Law
208 Dome DSSW20K, Roosevelt Island Climate Evolution (RICE), Dome Fuji (DF), EPICA (European Project
209 for Ice Coring in Antarctica) Dome C (EDC), and South Pole Ice Core (SPC14, or SP). Ice core locations
210 in Antarctica are shown in Fig. 2A. In Greenland, we use samples from the Greenland Ice Sheet Project 2
211 (GISP2).

212 We shall refer to late Holocene data from these sites as the calibration dataset, analogous to a core top data
213 set in the sediment coring literature. Site characteristics, coordinates, and number of samples included in
214 the calibration data set are given in Table 1. The DE08-OH site is a recent revisit of the Law Dome DE08
215 site. The DE08-OH core was measured at sub-annual resolution to understand cm-scale $^{86}\text{Kr}_{\text{ex}}$ variations
216 due to for example layering in firn density and bubble trapping (Appendix B). In addition to the calibration
217 data set, we present a record of Kr-86 excess going back to the LGM from WDC.

218 2.2 Ice sample analysis

219 We broadly follow analytical procedures described elsewhere (Bereiter et al., 2018a; Bereiter et al., 2018b;
220 Headly and Severinghaus, 2007; Severinghaus et al., 2003). In short, an 800 g ice sample, its edges trimmed
221 with a band saw to expose fresh surfaces, is placed in a chilled vacuum flask that is then evacuated for 20
222 minutes using a turbomolecular pump. Air is extracted from the ice by melting the sample while stirring
223 vigorously with a magnetic stir bar, led through a water trap, and cryogenically trapped in a dip tube
224 immersed in liquid He. Next, the sample is split into two unequal fractions. The smaller fraction (about 2%
225 of total air) is analyzed for $\delta^{15}\text{N-N}_2$, $\delta^{18}\text{O-O}_2$, $\delta\text{O}_2/\text{N}_2$ and $\delta\text{Ar}/\text{N}_2$ on a 3kV Thermo Finnigan Delta V plus
226 dual inlet IRMS (isotope ratio mass spectrometer). In the larger fraction, noble gases are isolated via hot
227 gettering to remove reactive gases. The purified noble gases are then analyzed for $\delta^{40/36}\text{Ar}$, $\delta^{40/38}\text{Ar}$, $\delta^{86/82}\text{Kr}$,
228 $\delta^{86/84}\text{Kr}$, $\delta^{86/83}\text{Kr}$, $\delta\text{Kr}/\text{Ar}$ and $\delta\text{Xe}/\text{Ar}$ on a 10kV Thermo Finnigan MAT253 dual inlet IRMS. We reject
229 one sample from RICE due to incomplete sample transfer, and one sample from WDC due to problems
230 with the water trap. Calibration is done for each measurement campaign by running samples of La Jolla
231 pier air.

232 All calibration (core top) data were measured using “Method 2” as described by Bereiter et al. (2018a),
233 with a longer equilibration time during the splitting step than used in that study to improve isotopic
234 equilibration between the fractions. The exception is the DE08-OH site, where the ice sample (rather than
235 the extracted gas sample) was split into two fractions – the advantage of this approach is that it does not
236 require a gas splitting step that is time-consuming and may fractionate the isotopes; the downside is that
237 the samples may have slightly different isotopic composition due to the stochastic nature of bubble trapping
238 and the different gas-loss histories of the ice pieces.

239 Measurements of the WDC downcore data set were performed over five separate measurement campaigns
240 that occurred in February-April 2014, February-April 2015, August 2015, August 2020, and August 2021,

241 respectively. The first three campaigns are described by Bereiter et al. (2018b), in which the $^{86}\text{Kr}_{\text{xs}}$ data are
242 a by-product of measuring $\delta\text{Kr}/\text{N}_2$ for reconstructing global mean ocean temperature. Campaigns 1 and 2
243 are in good agreement, whereas campaign 3 appears offset from the other two by an amount that exceeds
244 the analytical precision (offset around 35 per meg ‰^{-1}). To validate the main features in the record, we
245 performed two additional campaigns (4 and 5), in which all the gas extracted from each ice sample was
246 quantitatively gettered and only analysed for Ar and Kr isotopic composition. The downcore record, as well
247 as the five analytical campaigns, are discussed in detail in section 5.1. Data from the bubble-clathrate
248 transition zone (here 1000 to ~~1500~~1600 m depth, or \sim 4ka to 7ka BP) are excluded owing to the potential
249 for artefacts—: the depth range of the bubble-clathrate transition zone is based on observed positive
250 anomalies in $\delta\text{O}_2/\text{N}_2$ in WDC ice.

251 All samples were analyzed at Scripps Institution of Oceanography, USA, with the exception of the EDC
252 samples which were analyzed at University of Bern, Switzerland (Baggenstos et al., 2019). Some of the
253 EDC samples analyzed had clear evidence of drill liquid contamination, which acts to artefactually lower
254 $^{86}\text{Kr}_{\text{xs}}$ via isobaric interference on mass 82; the late Holocene data used here were not flagged for drill liquid
255 contamination- (Baggenstos et al., 2019).

256 The 2σ analytical precision of the $\delta^{15}\text{N}$, $\delta^{40}\text{Ar}$, and $\delta^{86}\text{Kr}$ measurements is around 3, 5 and 26 per meg,
257 respectively, based on the reproducibility of La Jolla Air measurements. Via standard error propagation,
258 this results in a \sim 22 per meg ‰^{-1} (2σ) analytical uncertainty for both $^{86}\text{Kr}_{\text{xs}40}$ and $^{86}\text{Kr}_{\text{xs}157}$ at a site like
259 WDC where $\delta^{40}\text{Ar} \approx 1.2 \text{‰}$. We have no true (same-depth) replicates to assess the reproducibility of $^{86}\text{Kr}_{\text{xs}}$
260 measurements experimentally. The measured isotope ratios are corrected for gas loss (Δ_{GL}^{40}) and thermal
261 fractionation (Δ_{TF}^{36} , Δ_{TF}^{40} , Δ_{TF}^{55}) before interpretation; details on these corrections are given in appendix A.
262 For the coretop calibration study, the average magnitude of the gas loss and thermal fractionation
263 corrections is +14 and -15 per meg ‰^{-1} in $^{86}\text{Kr}_{\text{xs}}$, respectively. Note that these two corrections both involve
264 the $\delta^{40}\text{Ar}$ isotopic ratio, and therefore they are not independent from each other and not additive – in other
265 words, the total correction is not simply the sum of the two individual corrections.

266 Our study includes two ice cores from the Antarctic Peninsula: ~~BPBRP~~ (2 ice samples) and JRI (5 ice
267 samples). Measured $\delta\text{Xe}/\text{N}_2$ ratios (and to a lesser extent the $\delta\text{Kr}/\text{N}_2$ ratios) in all samples from both
268 locations are significantly elevated above the expected gravitational enrichment signal (Fig. A1A), which
269 is clear evidence for the presence of refrozen meltwater in these samples (Orsi et al., 2015). Like xenon,
270 krypton is highly soluble in (melt)water, and therefore $^{86}\text{Kr}_{\text{xs}}$ cannot be reliably measured in these samples;
271 we reject all samples from the ~~BPBRP~~ and JRI sites. It is notable that all samples from both sites show
272 evidence of refrozen meltwater, given that the high-accumulation ~~BPBRP~~ core is nearly entirely free of
273 visible melt layers, and that we carefully selected samples without visible melt features at JRI. Visible ice
274 lenses form only when meltwater pools and refreezes on top of low-permeability layers such as wind crusts;
275 our observations suggest meltwater can also refreeze throughout the firn in a way that cannot be detected
276 visually.

277

278 3 Calibrating Kr-86 excess

279 The $^{86}\text{Kr}_{\text{xs}}$ proxy for synoptic activity was first proposed on theoretical grounds by Buizert and
280 Severinghaus (2016) – here we provide the first experimental validation of this proxy using a coretop
281 calibration of $^{86}\text{Kr}_{\text{xs}}$ using late-Holocene ice core samples from nine locations around Antarctica and one in
282 Greenland that represent a wide range of pressure variability in the modern climate- ([here: 1979-2017 CE](#)).

283 3.1 Spatial variation in synoptic-scale pressure variability

284 Kr-86 excess is sensitive to air movement (both upward and downward), which in turn is controlled by the
285 magnitude of relative air pressure change. Let p_i be a time series of (synoptic-scale) site surface pressure
286 with N data points, time resolution Δt , and mean value \bar{p} . The time series can span a month, year, or multi-
287 year period, with \bar{p} potentially different for each month or year. We define the parameter Φ as:

$$288 \quad \Phi = \frac{1}{N\bar{p}} \sum_{i=1}^N \left| \frac{p_i - p_{i-1}}{\Delta t} \right| \quad (5)$$

289 which we here express in convenient units of $\% \text{ day}^{-1}$. Φ reflects the intensity of barometric pumping in the
290 firn column. Note that Δt should be larger than ~ 1 hour (the timescale for the entire firn column to
291 equilibrate with the surface pressure), and smaller than about a day (in order to adequately resolve synoptic-
292 scale pressure events). Here we use ERA-interim reanalysis data from 1979-2017 with $\Delta t = 6$ hours (Dee
293 et al., 2011), from which we calculate monthly and annual Φ values using Eq. (5). A map of annual-mean
294 Φ across Antarctica is given in Fig. 2A. At all sites considered, Φ has a strong seasonal cycle with pressure
295 variability/storminess being strongest in the local winter season (Fig. 2C). Interannual [variability differences](#)
296 in Φ [isare](#) greatest along the Siple coast and coastal West Antarctica (Fig. 2B), mainly reflecting the
297 influence of central Pacific (ENSO, PDO) climate variability (Section 4).

298 3.2 Kr-86 excess proxy calibration

299 Present-day Antarctica has a wide range of Φ (Fig. 2A), which allows us to validate and calibrate $^{86}\text{Kr}_{\text{xs}}$. In
300 Fig. 3A we plot the site mean $^{86}\text{Kr}_{\text{xs}40}$ (with $\pm 1\sigma$ error bars) as a function of [\$\Phi\$, \$\Phi\$ \(averaged over full 1979-](#)
301 [2017 period\)](#). We find a Pearson correlation coefficient of $r = -0.94$ when using site mean $^{86}\text{Kr}_{\text{xs}40}$, and $r =$
302 -0.83 when using the $^{86}\text{Kr}_{\text{xs}40}$ of individual samples, respectively ($p < 0.01$). Note that in this particular case
303 the site-mean $^{86}\text{Kr}_{\text{xs}40}$ and $^{86}\text{Kr}_{\text{xs}15}$ are identical (because by design, after thermal correction $\delta^{15}\text{N} = \delta^{40}\text{Ar}$);
304 the error bars are different, though.

305 The $^{86}\text{Kr}_{\text{xs}}$ data have been corrected for gas loss (Appendix A1) and thermal fractionation (Appendix A2);
306 with the gas loss correction being the more uncertain component. Figure 3B shows the correlations of the
307 calibration curve as a function of the gas loss scaling parameter ϵ_{40} . We find a good correlation over a wide
308 range of ϵ_{40} values, proving our calibration is not dependent on the choice of ϵ_{40} . When using uncorrected
309 $^{86}\text{Kr}_{\text{xs}40}$ data the site mean correlation is $r = -0.71$; when applied individually, both the gas loss and thermal
310 correction each improve the correlation to $r = -0.77$ and $r = -0.79$, respectively (Fig. A3, all $p < 0.05$). Based
311 on these tests we conclude that the observed relationship is not an artefact of the applied corrections. The
312 applied corrections improve the correlation, which increases confidence in the method. The calibration
313 results for $^{86}\text{Kr}_{\text{xs}15}$ are shown in Fig. A4.

314 Notably, there is a large spread in $^{86}\text{Kr}_{\text{xs}}$ across samples from any single site, particularly at the high- Φ
315 sites of SDM and RICE (Fig. 3A, note the $\pm 1\sigma$ error bars). This spread is larger than the measurement
316 uncertainty, and we believe this variance reflects a signal that is truly present in the ice. The Siple coast and
317 Roosevelt Island experience the largest Φ interannual variability differences in Antarctica (Fig. 2B), and it
318 is therefore likely that our coarse sampling is aliasing the true $^{86}\text{Kr}_{\text{xs}}$ signal. The variance in $^{86}\text{Kr}_{\text{xs}}$ may
319 contain climate information also; this is reminiscent of the way in which the variance (rather than the mean)
320 of $\delta^{18}\text{O}$ in individual planktic foraminifera in ocean sediment samples from the equatorial Pacific can be
321 used as a proxy for past ENSO variability (Koutavas et al., 2006).

322 Both theoretical considerations and observations thus suggest $^{86}\text{Kr}_{\text{xs}}$ is a proxy for time-averaged barometric
323 surface pressure variability at the site, and in the remainder of this manuscript we will interpret it as such.

324 3.3 Discussion of the Kr-86 excess proxy

325 Our interpretation of $^{86}\text{Kr}_{\text{xs}}$ as a proxy for time-averaged pressure variability is somewhat complicated by
326 the possibility of deep convective zones, which have the same $^{86}\text{Kr}_{\text{xs}}$ signature as barometric pumping. This
327 was discovered at the Megadunes (MD) site, central East Antarctica; at this zero-accumulation site deep
328 cracks form in the firn layer that facilitate a 23 m deep convection zone (Severinghaus et al., 2010). In fact,
329 this observation led earlier work to suggest that noble gas gravitational disequilibrium may be used as a
330 proxy for convective zone thickness (Kawamura et al., 2013), rather than synoptic-scale pressure variability
331 as suggested here. Although megadunes and zero-accumulation zones are ubiquitous and cover 20% of the
332 Antarctic Plateau (Fahnestock et al., 2000), ice cores are seldom drilled in these areas and it is safe to
333 assume that they never formed at sites like WAIS Divide that had relatively high accumulation rates even
334 during the last glacial period. Performing the corrections for thermal and size-dependent fractionation is
335 challenging at MD, and we suggest that the MD $^{86}\text{Kr}_{\text{xs}}$ is in the range of -2 to -55 per meg ‰^{-1} ; even at the
336 larger limit, this is still smaller in magnitude than $^{86}\text{Kr}_{\text{xs}}$ anomalies at several modern-day sites with small
337 convective zones (such as SDM, RICE and the Law Dome sites), suggesting barometric pumping is capable
338 of producing larger $^{86}\text{Kr}_{\text{xs}}$ signals than even the most extreme observed case of convective surface mixing.
339 Having $^{86}\text{Kr}_{\text{xs}}$ measured in MD ice core (rather than firn air) samples would be valuable for a more
340 meaningful comparison to the ice core sample measurements presented here. Windy sites can have
341 substantial convective zones of ~ 14 m (Kawamura et al., 2006), and future studies of $^{86}\text{Kr}_{\text{xs}}$ at such sites
342 would be valuable.

343 Currently, 1-D and 2-D firn air transport model simulations underestimate the magnitude of the $^{86}\text{Kr}_{\text{xs}}$ signal
344 compared to measurements in mature ice samples (Birner et al., 2018), complicating scientific
345 understanding of the proxy. In these models, the effective molecular diffusivity of each gas is scaled linearly
346 to its free air diffusivity. The ratio of krypton to argon free air diffusivity is 0.78. This ratio, which directly
347 sets the magnitude of the simulated $^{86}\text{Kr}_{\text{xs}}$, may actually be smaller than 0.78 in real firn, as krypton is more
348 readily adsorbed onto firn surfaces retarding its movement (similar to gasses moving through a gas
349 chromatography column). This may be one explanation for why models simulate too little $^{86}\text{Kr}_{\text{xs}}$.

350 Another likely explanation for the model-data mismatch is that certain critical sub-grid processes (such as
351 the aforementioned pore-size dependence of the Péclet number) are not adequately represented in these
352 models. Barometric pumping may further actively shape the pore network through the movement of water
353 vapor, thereby keeping certain preferred pathways connected and open below the density where percolation

354 theory would predict their closure (Schaller et al., 2017). The fate of a pore restriction is determined by the
355 balance between the hydrostatic pressure (that acts to close it) and vapor movement away from its convex
356 surfaces (that acts to keep it open); we speculate that barometric Darcy air flow keeps high-flow channels
357 connected longer by eroding convex surfaces. This enhances the complexity (and therefore dispersivity) of
358 the deep firn pore network and possibly creates a non-linear $^{86}\text{Kr}_{\text{xs}}$ response to barometric pumping. The
359 hypothesized channel formation in deep firn is driven by a positive feedback on flow volume, and somewhat
360 reminiscent of erosion-driven stream network formation in fluvial geomorphology.

361 Firn models predict that, after correcting for thermal fractionation, the deviation from gravitational
362 disequilibrium effect inequilibrium for the elemental ratios (such as $\delta\text{Kr}/\text{Ar}$) should be proportional to that
363 deviation in isotopic ratios. However, the observations suggest that the former is usually smaller than would
364 be expected from the latter. We do not have an explanation for As before, adsorption of Kr onto firn grain
365 surfaces may contribute to the observed discrepancy, and laboratory tests of this effect-process are called
366 for. Further, the impacts of gas loss are greater on elemental ratios than on the isotopic ratios which may
367 contribute also. Including measurements of xenon isotopes and elemental ratios in future measurement
368 campaigns may be able to provide additional constraints to better understand this discrepancy.

369 Measurements on firn air samples, where available, suggest a smaller $^{86}\text{Kr}_{\text{xs}}$ anomaly in firn air than found
370 in ice core samples from the same site. We attribute this in part to a seasonal bias that is introduced by the
371 fact that firn air sampling always takes place during the summer months, whereas the synoptic variability
372 that drives the Kr-86 excess anomalies is largest during the winter (Fig. 2C); consequently, firn air
373 observations are biased towards weaker $^{86}\text{Kr}_{\text{xs}}$. Further, in the deep firn where $^{86}\text{Kr}_{\text{xs}}$ anomalies are largest,
374 firn air pumping may not yield a representative air sample, but rather be biased towards the well-connected
375 porosity at the expense of poorly-connected cul-de-sac-like pore clusters. Since barometric pumping
376 ventilates this well-connected porespace with low- $^{86}\text{Kr}_{\text{xs}}$ air from shallower depths, the firn air sampling
377 may not capture a representative $^{86}\text{Kr}_{\text{xs}}$ value of the full firn air content. These explanations are all somewhat
378 speculative, and a definitive understanding of the firn-ice differences is lacking at this stage.

379 Gas loss and thermal corrections are critical to the interpretation of $^{86}\text{Kr}_{\text{xs}}$. The thermal correction is applied
380 to account for thermal gradients in the firn (ΔT , here defined as the temperature at the top minus the
381 temperature at the base of the firn), which are chiefly caused by geothermal heat or surface temperature
382 changes at the site. At low-accumulation sites geothermal heating leads to $\Delta T < 0$. We use ^{15}N -excess ($\delta^{15}\text{N}$
383 $- \delta^{40}\text{Ar}/4$) to estimate the thermal gradient in the firn (Appendix A2). Because nitrogen and argon have
384 similar diffusivities but different thermal diffusion coefficients, $\delta^{15}\text{N} - \delta^{40}\text{Ar}$ is relatively insensitive to
385 barometric pumping yet sensitive to thermal fractionation, allowing estimating ΔT .

386 Besides the actual thermal gradients in the firn, the isotopic composition may also be impacted by seasonal
387 rectifier effects. If the firn air transport properties differ between the seasons (for example due to thermal
388 contraction cracks, convective instabilities, or seasonality in wind pumping), this can result in a thermal
389 fractionation of isotopic ratios in the absence of a thermal gradient (Morgan et al., 2022).

390 For the WDC, DSS and GISP2 sites we obtain ΔT values close to zero as expected for these high-
391 accumulation sites; for the SP, SDM, RICE, and DF sites we find ΔT ranging from -0.76 to -1.18°C, in
392 agreement with the effect of geothermal heat. The high-accumulation DE08 and DE08-OH sites both have

393 an unexpectedly large ΔT of -1.6°C ; the good agreement between the sites suggest it is likely a real signal,
394 yet we can rule out geothermal heat as the cause. This may suggest that the Law Dome DE08 site is subject
395 to a seasonal rectifier effect, or a recent climatic cooling. Last, the EDC site shows an unexpected $\Delta T =$
396 $+1.6 \pm 1.89^\circ\text{C}$. Three possible explanations are: (1) the aforementioned drill liquid contamination for this
397 core; (Baggenstos et al., 2019); (2) a summertime-biased seasonal rectifier; or (3) an over-correction of
398 $\delta^{40}\text{Ar}$ for gas loss, which could occur for example if natural and post-coring fugitive gas loss fractionate
399 $\delta^{40}\text{Ar}$ differently and EDC samples were impacted mostly by the former type (our correction is mostly
400 based on measurements of the latter type).

401 For the Law Dome DE08-OH site we observe large (5-fold) sub-annual variations in $^{86}\text{Kr}_{\text{xs}}$ (Fig. B1). The
402 magnitude of the $^{86}\text{Kr}_{\text{xs}}$ layering is truly remarkable. The isotopic enrichment of each gas ($\delta^{15}\text{N}$, $\delta^{40}\text{Ar}$,
403 $\delta^{86}\text{Kr}$) can be converted to an effective diffusive column height (DCH). For the samples with the smallest
404 (greatest) $^{86}\text{Kr}_{\text{xs}}$ magnitude, this DCH is around 1 m (6 m) shorter for $\delta^{86}\text{Kr}$ than it is for $\delta^{15}\text{N}$. The firm air
405 transport physics that may explain such phenomena are beyond our current scientific understanding. The
406 sub-annual variations may be related to the seasonal cycle in storminess (Fig. 2C), though that seems
407 improbable to us at present as the gas age distribution at the depth of bubble closure has a width of several
408 years (Schwander et al., 1993). Another reason may be seasonal layering in firm properties – such as density,
409 grain size, and pore connectivity – that control the degree of disorder and dispersive mixing occurring in
410 the firm, and lead to a staggered firm trapping and seasonal variations in Δage (Etheridge et al., 1992; Rhodes
411 et al., 2016). The sample air content estimated from the IRMS inlet pressure is similar for all measurements,
412 making it unlikely that the variations in $^{86}\text{Kr}_{\text{xs}}$ are caused by remnant open porosity in lower-density layers.
413 In any case it is remarkable that such large variations in gas composition can arise and persist on such small
414 length scales, given the relatively large diffusive, dispersive, and advective transport length scales of the
415 system. More work is needed to establish the origin of the sub-annual variations in ice core $^{86}\text{Kr}_{\text{xs}}$. At all
416 other sites analyzed here, the sample length exceeds the annual layer thickness; this will remove some, but
417 not all, of the effects of the sub-annual variations.

418 Another puzzling observation is the positive $^{86}\text{Kr}_{\text{xs}}$ at the Dome Fuji (DF) site; theoretical considerations
419 suggest it should always be negative. In part this may be due to an over-correction of $\delta^{40}\text{Ar}$ for gas loss,
420 which would act to bias $^{86}\text{Kr}_{\text{xs}}$ in the positive direction. This correction is largest at DF owing to the very
421 negative $\delta\text{O}_2/\text{N}_2$ and $\delta\text{Ar}/\text{N}_2$ (Fig. A1); while we base our correction on published work, it is conceivable
422 that we overestimate the true correction (Appendix A1). In particular, our gas loss correction is based on
423 observations on artefactual post-coring gas loss, which may fractionate $\delta^{40}\text{Ar}$ differently than natural
424 fugitive gas loss during bubble close-off. Omitting the gas loss correction indeed makes $^{86}\text{Kr}_{\text{xs}}$ at DF
425 negative (Fig. A3C-D). Another hypothesis is that the positive $^{86}\text{Kr}_{\text{xs}}$ signal is an artefact of the seasonal
426 rectifier that Morgan et al. (2022) identify at DF. In this work we assume a linear approach in which the
427 effect of the rectifier can be described by a single ΔT value that is the same for isotopic pairs. In reality,
428 there may be non-linear interactions between thermal fractionation and firm advection that impact the
429 isotopic values of the various gases in a more complex way than captured in our approach.

430 The $^{86}\text{Kr}_{\text{xs}}$ is also correlated with other site characteristics besides Φ . For site elevation we find $r = 0.96$
431 (0.84); and for mean annual temperature $r = -0.87$ (-0.76); the number in parentheses gives the correlation
432 when using all the individual samples rather than site-mean $^{86}\text{Kr}_{\text{xs}}$. The listed correlations all have $p < 0.01$.
433 For site accumulation we do not find a statistically significant correlation at the 90% confidence level. The

434 correlations with elevation and temperature are comparable to those we find for Φ ; this is no surprise given
435 that elevation, Φ and T are all strongly correlated with one another, mainly because elevation directly
436 ~~controls~~impacts both T (via the lapse rate) and Φ (~~by limiting via its topographic influence on the~~
437 ~~penetration position of storms~~storm tracks). To our knowledge there are no mechanisms through which
438 either elevation or annual-mean temperature could drive kinetic isotopic fractionation in the firn layer.
439 Perhaps other unexamined site characteristics (such as the degree of density layering, or the magnitude of
440 the annual temperature cycle) could provide good correlations also, suggesting additional hidden controls
441 on $^{86}\text{Kr}_{\text{xs}}$. The data needed to assess such hidden controls are not available for most sites.

442 The calibration of the $^{86}\text{Kr}_{\text{xs}}$ proxy is based on spatial regression. In applying the proxy relationship to
443 temporal records, we make the implicit assumption that proxy behavior in the temporal and spatial
444 dimensions is at least qualitatively similar. This assumption may prove incorrect. In particular, changes in
445 insolation are known to impact firn microstructure and bubble close-off characteristics, which in turn
446 impacts gas records of $\delta\text{O}_2/\text{N}_2$ and total air content (Bender, 2002; Raynaud et al., 2007). Since $^{86}\text{Kr}_{\text{xs}}$ is
447 linked to the dispersivity of deep firn, it seems probable that insolation has a direct impact on $^{86}\text{Kr}_{\text{xs}}$ also via
448 the firn microstructure. We will revisit this issue in our interpretation of the ~~WBWDC~~WDC $^{86}\text{Kr}_{\text{xs}}$ record (Section
449 5). Overall, we anticipate $^{86}\text{Kr}_{\text{xs}}$ to be a qualitative proxy for synoptic variability, yet want to caution against
450 quantitative interpretation based on the spatial regression slope.

451 The observations presented in this section clearly highlight the fundamental shortcomings of our current
452 understanding of firn air transport hinting at the existence of complex interactions, presumably at the pore-
453 scale, that are not being represented. Percolation theory finds that near the critical point (presumably the
454 lock-in depth) a network becomes fractal in its nature; we suggest that this fractal nature of the pore network
455 likely contributes to non-linear pore-scale interactions that give rise to the $^{86}\text{Kr}_{\text{xs}}$ observations in ice. While
456 the observed correlation of Fig. ~~3C3A~~3C3A is highly encouraging, further work is critical to understand this
457 proxy. Examples of such future studies are: (1) additional high-resolution records that can resolve the true
458 variations that exist in a single ice core, similar to the DE08-OH record; (2) 3-D firn air transport model
459 studies; (3) improvements to the gas loss correction; (4) additional coring sites to extend the spatial
460 calibration and further confirm the validity of the proxy; (5) Adding xenon isotopic constraints (^{136}Xe
461 excess) as an additional marker of isotopic disequilibrium; (6) numerical simulations of pore-scale air
462 transport in large-scale firn networks; (7) experimental studies of dispersion and noble gas adsorption in
463 firn samples; ~~and~~ (8) percolation theory approaches to study the fractal nature of the pore network of the
464 lock-in zone; and (9) replication of the WDC deglacial $^{86}\text{Kr}_{\text{xs}}$ record in nearby ice cores such as RICE.

465 **4 Present-day controls on Kr-86 excess in Antarctica**

466 In this section we investigate the large-scale patterns of climate variability in the Southern Hemisphere that
467 could affect Φ and therefore $^{86}\text{Kr}_{\text{xs}}$ over Antarctica. We begin by investigating the patterns in the wind field
468 that are associated with changes in Φ at ice core sites, before examining how more canonical patterns of
469 Southern Hemisphere climate variability, such as the southern annular mode (SAM), might affect Φ over
470 the whole of Antarctica.

471 We use ERA-interim reanalysis data for the 1979-2017 period (Dee et al., 2011) to evaluate the present-
472 day controls on synoptic-scale pressure variability in Antarctica. Kr-86 excess in an ice core sample
473 averages over several years of pressure variability, and therefore we focus on annual-mean correlation in
474 our analysis. The annual-mean Φ is calculated from the 6-hourly reanalysis data using Eq. (5). Note that
475 we let the year run from April to March to avoid dividing single El Niño / La Niña events across multiple
476 years.

477 At all Antarctic sites investigated, a similar pattern exists; four representative locations are shown in Fig.
478 4, where we regress the zonal wind in the lower (850 hPa, color shading) and upper troposphere (200 hPa,
479 contours) onto our surface pressure variability parameter Φ . We find that synoptic pressure variability at
480 these sites is linked to zonal winds along the southern margin of the eddy-driven subpolar jet (SPJ), which
481 extends from the surface to the upper troposphere (Nakamura and Shimpo, 2004; Trenberth, 1991). Sites
482 near the ice sheet margin (Figs. 4A, B and D) are most sensitive to the SPJ edge in their sector of Antarctica,
483 whereas interior sites (Fig. 4C) appear sensitive to the overall strength/position of the SPJ. Note that
484 strengthening, broadening or southward shifting of the SPJ all can in principle enhance site Φ .

485 Pressure variability at WDC is furthermore correlated with the strength of the Pacific Subtropical jet (STJ)
486 aloft (solid contour lines centered around 30°S in the Pacific in panel 4A), forming an upper troposphere
487 wind pattern that resembles the wintertime South Pacific split jet (Bals-Elsholz et al., 2001; Nakamura and
488 Shimpo, 2004); this agrees with the finding that a strengthening of the split jet enhances storminess over
489 West Antarctica (Chiang et al., 2014).

490 Next, we investigate how the well-known patterns of large-scale atmospheric variability, such as SAM and
491 ENSO, impact pressure variability in Antarctica. Figure 5 shows the correlation of Φ with the three leading
492 modes of SH extra-tropical atmospheric variability; the correlation with various indices and modes for
493 individual ice core locations is given in Table 2. Most teleconnection patterns have a specific season during
494 which they are strongest; here we do not differentiate between seasons, because $^{86}\text{Kr}_{\text{xs}}$ in ice core samples
495 averages over all seasons.

496 Globally, annual-mean Φ is highest over the Southern Ocean (Fig. 5A); a region of enhanced baroclinicity
497 associated with the eddy-driven SPJ (Nakamura and Shimpo, 2004). The green line denotes the latitude of
498 maximum Φ , corresponding roughly to the latitude with the highest storm track density (57.8°S on
499 average).

500 The dominant mode of atmospheric variability in the SH extratropics is the southern annular mode,
501 representing the vacillation of atmospheric mass between the mid- and high-latitudes (Thompson and
502 Wallace, 2000). Figure 5B shows 500 hPa geopotential height (Z500) anomalies associated with the SAM

503 as contours, with the color shading giving the correlation between Φ and the SAM index. During the
504 positive SAM phase (negative Z500 over Antarctica) we find that the stormtracks and maximum synoptic
505 activity are displaced towards Antarctica (positive Φ correlation poleward of the green line in Fig. 5B).
506 This is associated with a strengthening and poleward displacement of the SH westerly winds that occurs
507 during a positive SAM phase. More locally, Φ on the Antarctic Peninsula is positively correlated with the
508 SAM-index (Table 2); Φ at the other sites is not meaningfully impacted. This suggests that the variations
509 associated with the SAM (as commonly defined) do not extend far enough poleward to meaningfully impact
510 Antarctica with the exception of the Peninsula. Enhanced synoptic variability on the Peninsula during
511 positive SAM phases is consistent with observations of enhanced snowfall at those times (Thomas et al.,
512 2008).

513 The second mode of SH extratropical variability is the Pacific-South American Mode 1 (PSA1), which
514 reflects a Rossby wave response to sea surface temperature (SST) anomalies over the central and eastern
515 equatorial Pacific (Mo and Paegle, 2001), and is therefore closely linked to ENSO on interannual time
516 scales (we find a correlation of $r = 0.77$ between the annual mean PSA1 and Niño 3.4 indices). Φ in the
517 Amundsen and Ross Sea sectors (WDC, SDM and RICE) is positively correlated to the PSA1 and Niño 3.4
518 SST, suggesting larger synoptic activity during El Niño phases and low activity during La Niña phases. The
519 PSA2 pattern, also linked to SST anomalies in the tropical Pacific (Mo and Paegle, 2001), is likewise
520 correlated to Φ in the Amundsen and Ross Sea sectors (Fig. 5C and Table 2). While all the correlations
521 listed are statistically significant, they explain only a fraction of the total variability.

522 Next, we consider anomalies in sea ice area and extent (Parkinson and Cavalieri, 2012). We focus on the
523 Ross and Amundsen-Bellingshausen Seas where impacts on WAIS Divide may be expected. At the 90%
524 confidence level we do not find significant correlations to sea ice area or extent at most core locations
525 (Table 2). Correlations to sea ice extent are (even) weaker than those for sea ice area and consequently not
526 shown. We performed a lead-lag study of the correlations between Φ and sea ice area/extent in the various
527 sectors, and find that in all cases maximum correlations occur for the sea ice changes lagging 0 to 4 months
528 behind Φ ; we interpret this to mean that the sea ice is responding to changes in atmospheric circulation,
529 rather than driving them.

530 Overall, we find that synoptic activity at WAIS Divide, the site of most interest here, is controlled by the
531 position and/or strength of the stormtracks at the southern edge of the SPJ in the Pacific sector of the
532 Southern Ocean (Ross, Amundsen and Bellingshausen Seas), with little sensitivity to the SPJ behavior in
533 the other sectors. Owing to its remote southern location, WDC is only weakly impacted by the commonly-
534 defined large-scale modes of atmospheric variability. Most notably, WDC has a modest influence from the
535 tropical Pacific climate, as shown by a correlation around $r \approx 0.3$ to the PSA1, Niño 3.4 and PDO indices
536 (Table 2). We further find statistically significant correlations (up to $r = 0.44$) between WDC Φ and SST
537 in broad regions of the central and eastern tropical Pacific (not shown). We suggest that ENSO weakly
538 impacts storminess at WDC (around 10% of variance explained) via its impact on the SPJ in the South
539 Pacific.

540 **5 Barometric variability in West Antarctica during the last deglaciation**

541 **5.1 The 0-24 ka WAIS Divide Kr-86 excess record**

542 The WAIS Divide downcore $^{86}\text{Kr}_{\text{xs}}$ dataset we present here was produced during five separate measurement
543 campaigns that occurred in February-April 2014, February-April 2015, August 2015, August 2020, and
544 August 2021, respectively. Campaigns 1-3 were reported previously (Bereiter et al., 2018a; Bereiter et al.,
545 2018b), and campaigns 4 and 5 were meant to resolve conflicts between the $^{86}\text{Kr}_{\text{xs}}$ data sets from these
546 earlier campaigns. Three slightly different measurement approaches were used. Campaign 1 uses “Method
547 1” from Bereiter et al. (2018a), in which the air sample splitting is done in a water bath for over 12 hours
548 to equilibrate the sample. Campaigns 2 and 3 use “Method 2” from Bereiter et al. (2018a), in which a
549 bellows is used to split the air samples for over 4 to 6 hours. Campaigns 4 and 5 do not involve splitting of
550 the air sample, and only analyzed the Kr and Ar isotopic ratios. During campaign 4 a glass bead from the
551 water trap had gotten stuck in the tubing, restricting the flow and likely resulting in incomplete air extraction
552 from the melt water.

553 Figure 6 compares $^{86}\text{Kr}_{\text{xs}40}$ (panel A) and $^{86}\text{Kr}_{\text{xs}15}$ (panel B) from the five campaigns. Campaign 1 is the
554 only campaign that spans the full age range of the record, making it the most valuable of the three
555 campaigns. Campaigns 2 and 3 are mostly restricted to the Pleistocene and Holocene periods respectively,
556 with little overlap between them. Campaigns 4 and 5 aimed to reproduce some of the most salient features
557 in the earlier three.

558 No true replicate samples were analyzed between the campaigns, in part because the large sample size
559 requirement precludes this. To assess offsets, we rely on nearest-neighbor linear interpolation. We find an
560 offset of 5 per meg between the first and second campaign (during their period of overlap); this is within
561 the analytical precision (22 per meg), suggesting these two campaigns are in good agreement. The
562 agreement is good for both the $^{86}\text{Kr}_{\text{xs}40}$ and $^{86}\text{Kr}_{\text{xs}15}$ definitions. The first downcore campaign furthermore
563 overlaps in depth with the WDC calibration dataset (gray data in Fig. 6); we find no offset between those
564 data sets either. Data from campaign 2 appear to have more scatter, possibly reflecting the shorter
565 equilibration time during sample splitting.

566 We combine data from the first two campaigns, and evaluate their offset to data from the other three
567 campaigns using nearest-neighbor linear interpolation. For campaigns 3, 4 and 5 we find an offset of -31,
568 -22 and -23 per meg $\%o^{-1}$ in $^{86}\text{Kr}_{\text{xs}40}$, respectively. For campaign 3 the offset is -34 per meg $\%o^{-1}$ in $^{86}\text{Kr}_{\text{xs}15}$.
569 It is remarkable that all three later campaigns are more negative in $^{86}\text{Kr}_{\text{xs}}$ than the first two. Campaign 3
570 shows the greatest offset (greater than analytical precision), and has more scatter in both $^{86}\text{Kr}_{\text{xs}}$ (Fig. 6) and
571 ^{15}N excess (Fig. A5), and less care was taken during this campaign that the IRMS conditions were stable.
572 The offset of campaign 4 may be attributed to the incomplete sample transfer due to the bead stuck in the
573 line. The offset in campaign 5 is hard to explain. The systematically more negative $^{86}\text{Kr}_{\text{xs}}$ of campaigns 4
574 and 5 may reflect sample storage effects, as these were measured 5-6 years after campaign 1 and 2. However
575 this would not explain the negative values of campaign 3. The good $^{86}\text{Kr}_{\text{xs}}$ agreement between DE08 and
576 DE08-OH, drilled 32 years apart, would also argue against large storage effects. For campaign 4 and 5 only
577 Ar and Kr isotope ratios were measured, and so we lack typical tracers of gas loss ($\delta\text{O}_2/\text{N}_2$ and $\delta\text{Ar}/\text{N}_2$.)

578 In the remainder of this paper we will interpret the combined data from campaigns 1 and 2, but with the
579 caveat that there is a persistent offset with later campaigns. However, the features we interpret are
580 corroborated by the later campaigns, if one takes the offset into account. To aid interpretation of the data,
581 we apply a Gaussian smoothing spline with a smoothing filter width that varies depending on the data
582 density (from 250-year width in the deglaciation itself where the data density is high, to 1750 years in the
583 Holocene and LGM where data density is low). To estimate the uncertainty in the smoothing spline we use
584 a Monte Carlo approach that considers uncertainty in (1) the gas loss correction, by randomly sampling ϵ_{40}
585 in the range of 0 to -0.008; (2) the thermal correction, by randomly scaling the thermal scenario (Fig. A5)
586 by a factor ranging from 0 to 2; and (3) analytical errors, by adding random errors to individual data points
587 drawn from a normal distribution with a 2σ width of 22 per meg. The $\pm 1\sigma$ uncertainty range with mean
588 value are shown as the gray envelope and center line in Fig. 6. We believe the following observations to be
589 robust:

- 590 • The Holocene shows a trend towards increasingly negative $^{86}\text{Kr}_{\text{xs}}$, suggesting a gradual increase in
591 synoptic activity toward the present. Minimum synoptic activity in West Antarctica occurs during the
592 early Holocene around 10 ka BP; the Monte Carlo study suggests $^{86}\text{Kr}_{\text{xs}40}$ in the early Holocene (8ka-
593 10ka BP) is 30.5 ± 18 per meg $\%^{-1}$ ($\pm 2\sigma$) below the late-Holocene value (last 2 ka). Using the slope of
594 our core-top calibration (Fig. 3), we estimate that early-Holocene WDC synoptic activity Φ is $\sim 17\%$
595 weaker than it is today. This change is comparable to the 2σ magnitude of interannual variations in
596 annual mean Φ at the site today (or about half the peak-to-peak variations thereof). This Holocene trend
597 is seen in the data from campaigns 1, 3 and 4; ~~campaign~~. Campaign 5 does not suggest a trend but has
598 only one late Holocene data point making it less robust. The trend in campaign 3 is less robust due to
599 the greater scatter in the data.
- 600 • The most pronounced change occurs at the Younger Dryas (YD) - Holocene transition, where $^{86}\text{Kr}_{\text{xs}}$
601 becomes more positive (by 30.1 ± 16 per meg $\%^{-1}$, comparing YD and early Holocene) implying a
602 decrease in synoptic activity. This transition is observed in campaigns 1, 2, 4 and 5 that cover this time
603 period (the third campaign does not cover it), and represents a $\sim 17\%$ drop in synoptic activity (Φ).
- 604 • During the Last Glacial Maximum (LGM), WDC synoptic activity was perhaps slightly weaker than at
605 present, but not significantly so ($^{86}\text{Kr}_{\text{xs}40}$ more positive by 11 ± 13 per meg $\%^{-1}$). The West Antarctic
606 ice sheet elevation was likely higher during the LGM, and a 300 m elevation increase would by itself
607 increase $^{86}\text{Kr}_{\text{xs}40}$ by 10 per meg $\%^{-1}$, all else being equal (Appendix A3-); this is within the analytical
608 error of our observations. This feature is seen in campaign 1 and not covered by the other campaigns.
- 609 • The deglaciation itself has enhanced synoptic activity, in particular during the two North-Atlantic cold
610 stages Heinrich Stadial 1 (HS1) and the YD as highlighted with yellow bars in Figs. 6 and 7. Synoptic
611 activity during these periods is enhanced relative to the adjacent LGM and early Holocene, yet
612 comparable to today. This feature is seen in campaigns 1 and 2, and in 4 and 5 for the transition into
613 the Holocene.

614 Below we will interpret the deglacial ~~WDC~~ $^{86}\text{Kr}_{\text{xs}}$ record in terms of time-averaged barometric
615 variability. Before doing so we want to emphasize that firm processes may have been imprinted onto the
616 record also, in particular on orbital timescales where firm microstructure responds to local (summer)
617 insolation intensity (Bender, 2002). High summer insolation results in more depleted $\delta\text{O}_2/\text{N}_2$ and reduced
618 air content, likely via stronger layering and a delayed pore close-off process (Fujita et al., 2009).

619 Local summer solstice insolation in Antarctica increases through the Holocene, with the highest values in
620 the late Holocene. This may impact $^{86}\text{Kr}_{\text{xs}}$, although it is not a-priori clear what the sign of this relationship
621 would be. The sense of the Holocene temporal trends is that a more negative $^{86}\text{Kr}_{\text{xs}}$ coincides with more
622 negative $\delta\text{O}_2/\text{N}_2$. Note that this is opposite to the trends seen in the spatial calibration, where sites with the
623 most negative $\delta\text{O}_2/\text{N}_2$ (DF, SP, EDC) have the most positive $^{86}\text{Kr}_{\text{xs}}$. For now, the impact of local insolation
624 on $^{86}\text{Kr}_{\text{xs}}$ via firn microstructure remains unknown, which is an important caveat in interpreting the orbital-
625 scale changes in WDC $^{86}\text{Kr}_{\text{xs}}$. The abrupt $^{86}\text{Kr}_{\text{xs}}$ increase at the Holocene onset is too abrupt to be caused
626 by insolation changes, and thus we can interpret that change with more confidence.

627 The scatter in the late Holocene WDC $^{86}\text{Kr}_{\text{xs}}$ data exceeds the stated analytical precision. Potential
628 explanations include (1) an underestimation of the true analytical precision; (2) interannual to decadal
629 variations in storminess at WDC; and (3) aliasing of cm-scale variations in ice core $^{86}\text{Kr}_{\text{xs}}$ linked to layering
630 in firn microstructural properties.

631 **.5.2 Barometric variability at WAIS Divide during the last deglaciation**

632 In the present-day, synoptic-scale pressure variability at WAIS Divide is correlated with zonal wind
633 strength along the southern margin of the SPJ (Section 4). In our interpretation, a more negative $^{86}\text{Kr}_{\text{xs}}$
634 reflects a strengthening or southward shift of the SPJ in the Pacific sector. Here we provide a climatic
635 interpretation of the deglacial WDC $^{86}\text{Kr}_{\text{xs}}$ record, and suggest that variations in synoptic variability at WDC
636 are linked to meridional movement of the ITCZ on millennial and orbital timescales.

637 The main features of the deglacial WDC $^{86}\text{Kr}_{\text{xs}}$ record listed in Section 5.1 resemble similar features seen
638 in records of (sub-) tropical hydrology and monsoon strength, such as the speleothem calcite $\delta^{18}\text{O}$ records
639 from Hulu Cave, China (Fig. 7C) and from Botuvera cave, southern Brazil (Fig. 7D), which are thought to
640 reflect the intensity of the East Asian and South American summer monsoons, respectively (Cruz et al.,
641 2005; Wang et al., 2007; Wang et al., 2001). These two monsoon records are anti-correlated, showing
642 opposing rainfall trends between the NH and SH on both orbital and millennial timescales. This pattern is
643 commonly attributed to displacement of the mean meridional position of the ITCZ (Chiang and Friedman,
644 2012; McGee et al., 2014; Schneider et al., 2014), driven by hemispheric temperature differences (Fig. 7B).
645 On orbital timescales such ITCZ migration has a strong precessional component, moving towards the
646 hemisphere with more intense summer peak insolation; on millennial timescales the ITCZ responds to
647 abrupt North-Atlantic climate change associated with the D-O and Heinrich cycles (Broccoli et al., 2006;
648 Chiang and Bitz, 2005; Wang et al., 2001), which are in turn linked to changes in meridional heat transport
649 by the Atlantic meridional overturning circulation, or AMOC (Lynch-Stieglitz, 2017; Rahmstorf, 2002).

650 Changes in mean ITCZ position have a strong influence on the structure and strength of the SH jets. During
651 periods when the NH is relatively cold (such as D-O stadials or periods with negative orbital precession
652 index) the ITCZ is displaced southward and the SH Hadley cell is weakened, thereby also weakening the
653 SH upper-tropospheric subtropical jet (Ceppi et al., 2013; Chiang et al., 2014). The reverse is also true, with
654 the ITCZ shifted northward during NH warmth, associated with a strengthening of the SH Hadley cell and
655 STJ. In a range of model simulations (Ceppi et al., 2013; Lee and Kim, 2003; Lee et al., 2011; Pedro et al.,
656 2018) the weakening of the SH STJ (as during NH cold) is furthermore accompanied by a strengthening
657 and/or southward shift of the SPJ/eddy-driven jet and SH westerly winds. Recently, ice core observations
658 have confirmed in-phase shifts in the position of the SHW occur during the D-O cycle in parallel to those

659 of the ITCZ (Buizert et al., 2018; Markle et al., 2017). Marine records of fluvial sediment runoff off the
660 Chilean coast suggest precession-phased movement of the South Pacific SPJ, again in parallel to the ITCZ
661 movement (Lamy et al., 2019).

662 While data and models thus appear to agree on this first-order zonal-mean circulation response, zonal
663 asymmetries may lead to divergent outcomes at individual locations, particularly in the Pacific sector of
664 Antarctica where WDC is located. While the Heinrich (i.e. NH cooling) simulations clearly show the
665 aforementioned zonal mean strengthening of the eddy driven jet (Lee et al., 2011), they also suggest a
666 weakening of the South Atlantic austral winter split jet (Chiang et al., 2014); in this weakened split jet
667 configuration the STJ and SPJ are weakened at the expense of a strengthened mid-latitude jet. Essentially
668 the literature presents us with two opposing hypotheses for the response of the South Pacific SPJ to ITCZ
669 migration. In the zonal-mean framework, meridional ITCZ migration is accompanied by a parallel shift
670 (and/or strengthening) of the SH SPJ/eddy-driven jet, suggesting an anti-correlation between ITCZ latitude
671 and Antarctic storminess (with weak synoptic activity as the ITCZ is shifted north). However, if zonal
672 asymmetries in the SPJ response are considered, storminess at WDC may actually have the opposite
673 relationship to ITCZ position, due to a proposed weakening (strengthening) of the split jet as the ITCZ
674 shifts south (north). Our $^{86}\text{Kr}_{\text{ice}}$ record implies that synoptic activity at WDC is anticorrelated with ITCZ
675 position, suggesting that the zonally symmetric SPJ response advocated by e.g. Ceppi et al. (2013)
676 dominates over the zonally asymmetric split jet response advocated by Chiang et al. (2014).

677 The present-day SAM is sometimes suggested as an analogue for past shifts in index reflects the meridional
678 position of the SHW and eddy-driven jet (Rind et al., 2001); during. During positive SAM phases the SHW
679 are displaced poleward, and during negative phases equatorward. The WDC Kr-86 excess record, combined
680 with our analysis of the present-day circulation (Fig. 4), implies Present-day month-to-month changes to the
681 position and/or strength of the southern edge of the SPJ. However, we find that the present-day in SAM
682 does not have a statistically significant impact on synoptic variability at WDC (Table 2). Perhaps the SAM
683 is not a good analogue for these past changes in circulation after all, in particular when considering the
684 impact of SHW shifts on Antarctic storminess. The present-day SAM represents index represent a mode of
685 internal variability, with anomalies persisting for only weeks to months – the timescale is longest in late
686 spring and early summer reflecting a stronger planetary wave–mean flow interaction (Simpson et al., 2011;
687 Thompson and Wallace, 2000). By contrast, the shifts in the ITCZ, and presumably the associated changes
688 to the SH jet structure, persist for centuries to millennia. Moreover, the atmospheric dynamics of the SAM
689 on millennial and the ITCZ-driven shifts in the SHW are very orbital timescales have a much longer lifetime
690 and different, with the latter dynamics, being driven from the tropics via hemispherically asymmetric
691 changes in Hadley cell and STJ strength. Therefore, present-day SAM internal variability is not expected
692 to be a good analogue for past changes in SHW position. We find that the present-day SAM month-to-
693 month internal variability mainly impacts synoptic variability over the Southern Ocean and does not have
694 a statistically significant WDC (Table 2). Such variability is likely to have occurred during other climatic
695 regimes also, possibly just centered around a mean SHW position that is displaced meridionally relative to
696 today. At first glance it may appear contradictory to state, as we do, that synoptic activity at WDC is not
697 sensitive to the SAM while also suggesting that during the last deglaciation synoptic activity at WDC is
698 linked to changes in the position of the SH eddy-driven jet and westerlies. Based on the considerations
699 above, both claims may be true without contradiction.

700 Besides secular changes to the SPJ position/strength linked to meridional ITCZ movement, WDC $^{86}\text{Kr}_{\text{xs}}$
701 may also have imprints from ENSO and tropical Pacific climate. Our analysis suggests a weak, but
702 statistically significant link to common ENSO indicators (Table 2). Increased synoptic activity at WDC is
703 linked to enhanced convection in the central and eastern tropical Pacific, which may be due to enhanced
704 frequency or intensity of El Niño events, or a mean climate state that is more El Niño-like; it seems likely
705 that the Pacific mean state and ENSO variability are strongly linked (Salau et al., 2012), and the distinction
706 may be irrelevant.

707 The key features of the WDC $^{86}\text{Kr}_{\text{xs}}$ record are compatible with paleo-ENSO changes commonly described
708 in the literature. A majority of Holocene ENSO reconstructions (Conroy et al., 2008; Driscoll et al., 2014;
709 Koutavas et al., 2006; Moy et al., 2002; Riedinger et al., 2002; Sadekov et al., 2013) and a wide range of
710 climate model simulations (Braconnot et al., 2012; Cane, 2005; Clement et al., 2000; Liu et al., 2000; Liu
711 et al., 2014; Zheng et al., 2008) all suggest weakened ENSO activity during the early and mid-Holocene, a
712 time with reduced WDC synoptic activity. For example, Fig. 7F shows the number of El Niño events per
713 century (with trend line) reconstructed from inorganic clastic laminae in sediments from Laguna
714 Pallacocha, Ecuador, a region strongly affected by ENSO (Moy et al., 2002). Likewise, it has been
715 suggested that the SST gradient between the West Pacific warm pool and East Pacific cold tongue was
716 enhanced during the mid-Holocene, perhaps indicating a more La Niña-like mean climate state (Koutavas
717 et al., 2002; Sadekov et al., 2013).

718 Going from the early Holocene to the Younger Dryas (YD), we observe a large increase in WDC synoptic
719 activity. Enhanced ENSO activity during Heinrich stadials is generally supported by climate model
720 simulations (Braconnot et al., 2012; Merkel et al., 2010; Timmermann et al., 2007), and by limited proxy
721 evidence for stadial periods more broadly (Stott et al., 2002). Enhanced ENSO variability during the
722 deglaciation is also found by Sadekov et al. (2013), although their record lacks the temporal resolution to
723 resolve the individual stages. The zonal SST gradient in the equatorial Pacific further reaches a minimum
724 during HS1, also consistent with higher El Niño intensity (Sadekov et al., 2013).

725 The observed variations in $^{86}\text{Kr}_{\text{xs}}$ and implied changes in WDC synoptic activity may thus have two
726 contributions: (1) ITCZ-driven changes to the South Pacific SPJ position, and (2) changes to ENSO activity.
727 Based on previous work, we argue these two amplify one another in driving WDC storminess, yet we expect
728 the former to make the larger contribution. To disentangle zonally-uniform changes to the SPJ from changes
729 specific to the Pacific sector (such as ENSO and the split jet), $^{86}\text{Kr}_{\text{xs}}$ records from different sectors of
730 Antarctica are needed. Replication of the deglacial and Holocene WDC $^{86}\text{Kr}_{\text{xs}}$ record presented here is also
731 a high priority, both at WDC itself and at the nearby SDM and RICE cores, to validate that the signals we
732 describe and interpret here are indeed real and regional in scale.

733 The position of the SHW during the LGM has been a topic of much scientific inquiry. Proxy data have been
734 interpreted to show a northward LGM shift of the SHW – with other scenarios, including no change at all,
735 not excluded by the data (Kohfeld et al., 2013). Such a shift is not supported by most climate models (Rojas
736 et al., 2009; Sime et al., 2013). Our $^{86}\text{Kr}_{\text{xs}}$ record suggests LGM synoptic activity in West Antarctica to be
737 comparable to today after accounting for site elevation effects- (the elevation effect on $^{86}\text{Kr}_{\text{xs}}$ is within the
738 analytical error). This would be consistent with a Pacific SPJ position similar to today. Note that our site is
739 mostly sensitive to the position of the southern edge of the SPJ, and cannot meaningfully constrain changes
740 to the seasonality, width, and/or northern edge of the stormtracks. Therefore, it is not a-priori clear whether

741 our observations can be extrapolated to more general statements about SHW position and strength during
742 the LGM. Our data suggest that SPJ movement follows insolation and the ITCZ position, and hence the
743 LGM period may not be a good target for studying SHW movement in the first place given that it has a
744 precession index similar to the present-day.

745 Changes to the SPJ and its associated westerly surface winds have implications for ocean circulation and
746 marine productivity in the Southern Ocean via wind-driven upwelling. Opal flux records from the Antarctic
747 zone (Fig. 7G), reflecting diatom productivity, are commonly interpreted as a proxy for such upwelling –
748 with enhanced upwelling during southward displacement of the SHW (Anderson et al., 2009). Here we
749 only show records from the Pacific sector, given we find WDC $^{86}\text{Kr}_{\text{xs}}$ to reflect purely local SPJ dynamics
750 (Fig. 4A). Both published records suggest enhanced upwelling during the deglaciation (Fig. 7G), consistent
751 with a southward-shifted Pacific SPJ and enhanced storminess at WDC. The record from core PS75/072-4
752 (blue curve) further indicates an increasing productivity trend through the Holocene (Studer et al., 2018),
753 which is accompanied by a rise in surface nitrogen availability (reconstructed from diatom-bound nitrogen
754 isotopic composition, not shown); this Holocene trend matches our finding of increasing WDC storminess
755 and, by inference, an increasingly southern position of the Pacific SPJ and SHW. We thus conclude that
756 our interpretation of WDC $^{86}\text{Kr}_{\text{xs}}$ reflecting SPJ movement in parallel with the ITCZ, is broadly consistent
757 with indicators of wind-driven upwelling in the Pacific Antarctic zone.

758 **6 Conclusions**

759 Here we present ~~and calibrate~~ a new gas-phase ice core climate proxy, Kr-86 excess, that reflects time-
760 averaged surface pressure variability at the site driven by synoptic activity. Surface pressure variability
761 weakly disturbs the gravitational settling and enrichment of the noble gas isotope ratios $\delta^{86}\text{Kr}$ and $\delta^{40}\text{Ar}$ via
762 barometric pumping. Owing to its higher diffusion coefficient, argon is less affected by this process than
763 krypton is, and therefore the difference $\delta^{86}\text{Kr}-\delta^{40}\text{Ar}$ is a measure of synoptic activity.

764 This interpretation is supported by a calibration study in which we measure $^{86}\text{Kr}_{\text{xs}}$ in late Holocene ice core
765 samples from eleven Antarctic and one Greenland ice core that represent a wide range of synoptic activity
766 in the modern climate. Two of the Antarctic cores were rejected due to clear evidence of refrozen melt
767 water. We find a strong correlation ($r = -0.94$ when using site mean data and $r = -0.83$ when using individual
768 samples, $p < 0.01$) between ice core $^{86}\text{Kr}_{\text{xs}}$ and barometric variability at the site, demonstrating the validity
769 of the new proxy.

770 Current limitations of the new $^{86}\text{Kr}_{\text{xs}}$ proxy are: (1) it requires relatively large and non-trivial corrections
771 for gas loss and thermal fractionation; (2) it is moderately sensitive to changes in convective zone thickness;
772 (3) firn air transport models cannot simulate the magnitude of $^{86}\text{Kr}_{\text{xs}}$ anomalies measured in ice samples;
773 (4) firn air samples show smaller $^{86}\text{Kr}_{\text{xs}}$ anomalies than ice samples from the same site do; (5) it may be
774 sensitive to the degree of density layering at the site, as a comparison of the nearby Law Dome DE08 and
775 DSSW20K cores suggests; (6) it does not work for warm sites that experience frequent melt; (7) the
776 measurement is challenging (with offsets observed between measurement campaigns), time consuming,
777 and needs large ice samples; and (8) long-term sample storage may impose data offsets. Due to these
778 limitations, we caution that any interpretation of temporal $^{86}\text{Kr}_{\text{xs}}$ changes remains speculative at present.

779 Using atmospheric reanalysis data, we show that synoptic-scale barometric variability in Antarctica is
780 primarily linked to the position and/or strength of the southern edge of the eddy-driven subpolar jet (SPJ,
781 also called polar front jet) with a southward SPJ displacement enhancing synoptic-scale surface pressure
782 variability in Antarctica. The commonly-defined modes of large-scale atmospheric variability, such as the
783 southern annular mode and the Pacific-South American pattern, impact Antarctic only weakly as they are
784 weighted towards the mid-latitudes; the exception is the Antarctic Peninsula, where synoptic activity is
785 well-correlated with the southern annular mode ($r = 0.68$). Sites in the Amundsen and Ross Sea sectors are
786 weakly linked to tropical Pacific climate and ENSO ($r = 0.31$ to $r = 0.43$).

787 We present a new record of $^{86}\text{Kr}_{\text{xs}}$ from the WAIS Divide ice core in West Antarctica, that covers the last
788 24ka including the LGM, deglaciation and Holocene. West Antarctic synoptic activity is slightly below
789 modern levels during the last glacial maximum (LGM); increases during the Heinrich Stadial 1 and Younger
790 Dryas North Atlantic cold periods; weakens abruptly at the Holocene onset; remains low during the early
791 and mid-Holocene (up to ~17% below modern), and gradually increases to its modern value. The WDC
792 $^{86}\text{Kr}_{\text{xs}}$ record resembles records of tropical hydrology and monsoon intensity that are commonly thought to
793 reflect the meridional position of the ITCZ; the sense of the correlation is that WDC synoptic activity is
794 weak when the ITCZ is in its northward position, and vice versa. We interpret the record to reflect
795 migrations of the eddy-driven SPJ in parallel with those of the ITCZ (Ceppi et al., 2013). Secondary
796 influences may come from tropical Pacific climate and ENSO activity. Our $^{86}\text{Kr}_{\text{xs}}$ record is consistent with
797 weakened ENSO activity (or a more La Niña-like mean state) during the mid- and early Holocene, and

798 enhanced ENSO activity during NH stadial periods – both these features have been described in the paleo-
799 ENSO literature. The inferred changes to the SPJ are broadly consistent with proxies that indicate enhanced
800 wind-driven upwelling in the Pacific Antarctic zone during NH cold stadial periods.

801 Kr-86 excess is a new and potentially useful ice core proxy with the ability to enhance our understanding
802 of past atmospheric circulation. More work to better understand this proxy is warranted, and presently the
803 conclusions of this paper should be considered as tentative. In particular, replication of the deglacial Kr-86
804 excess record presented here in nearby cores is needed before these results can be interpreted with
805 confidence. [A full list of suggested follow-up studies is given in section 3.3.](#) Despite the many challenges
806 of Kr-86 excess, its further development is worthwhile owing to the dearth of available proxies for
807 reconstructing SH extratropical atmospheric circulation.

808 **Appendix A: data corrections**

809 **A1 Gas loss correction**

810 Gas loss processes artificially enrich the $\delta^{40}\text{Ar}$ isotopic ratio used to calculate $^{86}\text{Kr}_{\text{xs}}$ (Kobashi et al., 2008b;
811 Severinghaus et al., 2009; Severinghaus et al., 2003). Figure A1B shows the relationships between the two
812 most common gas loss proxies $\delta\text{O}_2/\text{N}_2$ and $\delta\text{Ar}/\text{N}_2$ for all samples in the calibration dataset; we find a slope
813 close to the 2:1 slope commonly reported in the literature (Bender et al., 1995); the exception is the DE08-
814 OH site where the data fall on a 1:1 slope. Depletion in fugitive gases (such as O_2 and Ar) represents the
815 sum of losses during bubble closure in the firn (Bender, 2002; Huber et al., 2006; Severinghaus and Battle,
816 2006), and those during drilling, handling, storage, and analysis of the samples (Ikeda-Fukazawa et al.,
817 2005). The patterns are inconsistent with storage conditions alone – for example the DF and EDC cores
818 were stored very cold and SP drilled very recently; yet all three have strong $\delta\text{O}_2/\text{N}_2$ and $\delta\text{Ar}/\text{N}_2$ depletion.
819 Natural gas loss from the firn, as well as artefactual loss during drilling likely dominate the signal. The
820 DE08-OH samples were dry-drilled and suffered from poor ice quality for the most depleted samples, which
821 may explain the alternate 1:1 slope at the site (Appendix B); note though that a recent work suggests a $\sim 5:1$
822 slope for post-coring gas loss (Oyabu et al., 2021). The DE08-OH samples were also analyzed differently
823 from those at other sites, with $\delta\text{O}_2/\text{N}_2$ and $\delta\text{Ar}/\text{N}_2$ measurements performed on a separate smaller ice piece
824 (see section 2.2); the greater surface-to-volume ratio of such small samples may result in greater gas
825 fractionation while evacuating the sample flasks in the laboratory.

826 Severinghaus et al. (2009) hypothesize that the apparent 2:1 slope of $\delta\text{O}_2/\text{N}_2$ to $\delta\text{Ar}/\text{N}_2$ depletion is a
827 combination of two mechanisms: size-dependent fractionation during diffusion through the ice lattice, and
828 mass-dependent fractionation (such as molecular or Knudsen diffusion) within ice fractures. In this
829 interpretation, the exact slope would depend on the relative contribution of each process to the total gas
830 loss. It is improbable that both processes would occur in the same ratio at such a wide variety of sites; the
831 2:1 slope is thus more likely an attribute of the gas diffusion rate of gases through ice itself, which is strongly
832 size-dependent, and weakly mass-dependent (Battle et al., 2011).

833 Gas loss is well known to enrich ice samples in $\delta^{18}\text{O}-\text{O}_2$, and following Severinghaus et al. (2009) we plot
834 $\delta^{18}\text{O}$ (corrected for gravity and small atmospheric $\delta^{18}\text{O}_{\text{atm}}$ variations) against gravitationally-corrected
835 $\delta\text{O}_2/\text{N}_2$ in Fig. A1C. We find a slope of 3.5 per meg enrichment in $\delta^{18}\text{O}$ per ‰ of $\delta\text{O}_2/\text{N}_2$ gas loss. This is
836 less than values reported elsewhere (Severinghaus et al., 2009), but provides further evidence for mass-
837 dependent fractionation during gas loss. Our core top dataset further suggests a correlation between
838 $\delta^{40}\text{Ar} - 4 \times \delta^{15}\text{N}$ (a measure of $\delta^{40}\text{Ar}$ enrichment impacted by both thermal fractionation and gas loss) and
839 gravitationally corrected $\delta\text{Ar}/\text{N}_2$ (Fig. A1D), suggesting Ar loss leads to enrichment of the remaining $\delta^{40}\text{Ar}$.

840 Following Severinghaus et al. (2009), we assume that the $\delta^{40}\text{Ar}$ correction scales with gas loss indicator
841 ($\delta\text{O}_2/\text{N}_2 - \delta\text{Ar}/\text{N}_2$):

842
$$\Delta_{GL}^{40} = \epsilon_{40} \times (\delta\text{O}_2/\text{N}_2 - \delta\text{Ar}/\text{N}_2)|_{\text{gravcorr}} \quad (\text{A1})$$

843 with Δ_{GL}^{40} the isotopic gas loss correction on $\delta^{40}\text{Ar}$ and ϵ_{40} a scaling parameter. Note that gravitationally
844 corrected $\delta\text{O}_2/\text{N}_2$ and $\delta\text{Ar}/\text{N}_2$ data are used. Here we rely on data from the Antarctic Byrd ice core for a best

845 estimate of ϵ_{40} (Fig. A2); some samples from this core suffered extreme gas loss with $(\delta O_2/N_2 - \delta Ar/N_2)$ as
 846 low as -100%. This data set suggest $\epsilon_{40} = -0.008$, or 8 per meg $\delta^{40}Ar$ enrichment per ‰ of $(\delta O_2/N_2 - \delta Ar/N_2)$
 847 gas loss. Because of the 2:1 slope between $\delta O_2/N_2$ and $\delta Ar/N_2$, we find that $(\delta O_2/N_2 - \delta Ar/N_2) \approx \delta Ar/N_2$
 848 and therefore the coefficient ϵ_{40} would have a similar slope when regressed against $\delta Ar/N_2$ instead of
 849 $(\delta O_2/N_2 - \delta Ar/N_2)$.

850 The value of $\epsilon_{40} = -0.008$ agrees reasonably well with other studies. Kobashi et al. (2008) compare replicate
 851 sample pairs to back out gas loss, and find (statistically significant) correlations between $\delta^{40}Ar$ enrichment
 852 and $\delta Ar/N_2$ (again, which is similar to $\delta O_2/N_2 - \delta Ar/N_2$). Kobashi et al. (2008) find ϵ_{40} values of -0.006, -
 853 0.005 and +0.007, depending on the depth range and analytical campaign evaluated. The positive value is
 854 surprising, given that most observations, as well as theory, suggest ϵ_{40} should be negative – we consider
 855 this a spurious result given the weak $\delta^{40}Ar - \delta Ar/N_2$ correlation in that particular data set. The other two
 856 values of ϵ_{40} are in reasonable agreement with the Byrd value. For the Siple Dome ice core (Severinghaus
 857 et al., 2003), regressing $\delta^{40}Ar$ against $\delta Kr/Ar$ gives a slope of +0.007; this implies $\epsilon_{40} = -0.007$ in good
 858 agreement with our findings. Last, our coretop data suggest $\delta^{40}Ar$ enrichment with an ϵ_{40} value of -0.0072
 859 (Fig. A1D), also in good agreement with Byrd.

860 Given the uncertainty in the gas loss parameter, we verify that our results are valid for a wide range of ϵ_{40}
 861 values (Fig. 3B).

862 A2 Thermal correction

863 In the presence of a temperature gradient, thermal diffusion causes isotopic enrichment towards the colder
 864 location. The thermal diffusion sensitivity Ω in units of ‰K⁻¹ for the various gases is given as (Grachev
 865 and Severinghaus, 2003a, b; Kawamura et al., 2013):

$$866 \quad \Omega^{15} = \frac{8.656}{T} - \frac{1232}{T^2}$$

$$867 \quad \Omega^{40} = \frac{26.08}{T} - \frac{3952}{T^2}$$

$$868 \quad \Omega^{86} = \frac{5.05}{T} - \frac{580}{T^2}$$

869 We estimate the thermal gradient ΔT in the firn using N-15 excess (Severinghaus et al., 1998):

$$870 \quad \Delta T = \frac{{}^{15}N_{xs}}{\Omega^{15} - \Omega^{40}/4} = \frac{\delta^{15}N - (\delta^{40}Ar + \Delta_{GL}^{40})/4}{\Omega^{15} - \Omega^{40}/4} \quad (A2)$$

871 with Δ_{GL}^{40} the $\delta^{40}Ar$ gas loss correction from Eq. (A1). Positive values of ΔT indicate that the surface is
 872 warmer than the firn-ice transition. The ΔT then in turn allows us to estimate the thermal corrections:

$$873 \quad \Delta_{fF}^{15} = -\Omega^{15} \Delta T$$

$$\begin{aligned} \Delta_{TF}^{40} &= -\Omega^{40} \Delta T \\ \Delta_{TF}^{86} &= -\Omega^{86} \Delta T \end{aligned} \quad (\text{A3})$$

876 The samples from the calibration dataset are from the climatically stable late Holocene period, and typically
 877 close together in depth; the uncertainty in the ΔT estimation for individual samples therefore exceeds the
 878 temporal variability in ΔT . To reduce the uncertainty in the thermal correction we estimate ΔT for individual
 879 samples using Eq. (A2), and for each site average the available data to get a site-average firn temperature
 880 gradient $\overline{\Delta T}$. The thermal correction is then given by:

$$\begin{aligned} \Delta_{TF}^{15} &= -\Omega^{15} \overline{\Delta T} \\ \Delta_{TF}^{40} &= -\Omega^{40} \overline{\Delta T} \\ \Delta_{TF}^{86} &= -\Omega^{86} \overline{\Delta T} \end{aligned} \quad (\text{A4})$$

884 The two methods are compared in Figs. A3C (individual sample ΔT) and A3D (site mean $\overline{\Delta T}$); it is clear
 885 that the $\overline{\Delta T}$ approach reduces the spread in $^{86}\text{Kr}_{\text{xs}}$ (error bars), but not its mean (white dots). The ΔT estimates
 886 in individual samples are subject to errors in the isotopic measurements; some of these errors will cancel
 887 out in the $\overline{\Delta T}$.

888 For the downcore WDC record through the deglaciation we can no longer assume a stationary ΔT ; we
 889 instead rely on dynamic firn densification model simulations of ΔT (Buizert et al., 2015). A comparison of
 890 the simulated and data-based ΔT is shown in Fig. A5 for WDC. The data clearly show a lot more
 891 scatter/variability than the simulations do. We interpret this mainly as analytical noise in the $\delta^{15}\text{N}$ and $\delta^{40}\text{Ar}$
 892 measurements, however, the gas loss correction (Appendix A1) also impacts the ΔT estimation in individual
 893 samples. The comparison suggests that the scatter in the ΔT estimates actually exceeds the magnitude of
 894 the simulated thermal signals. Using ΔT of the individual samples would thus introduce much scatter in the
 895 (thermally corrected) $^{86}\text{Kr}_{\text{xs}}$ records, and we choose to use the modelled ΔT instead.

896 A3 Elevation correction

897 To correct the deglacial WAIS Divide record for elevation changes, we here estimate the $^{86}\text{Kr}_{\text{xs}}$ dependence
 898 on site elevation using the calibration dataset. Note that elevation and synoptic activity are strongly
 899 correlated for the investigated sites ($r = -0.86$), with synoptic activity decreasing with elevation because
 900 the cyclonic systems do not penetrate deeply into the Antarctic interior. Figure A6 shows the result of this
 901 exercise. We find a slope of 34 per meg $\%_{\text{‰}}\%_{\text{‰}}^{-1}$ of $^{86}\text{Kr}_{\text{xs}}$ per 1000 m of elevation change, with a correlation
 902 of $r = 0.96$ when considering site-mean $^{86}\text{Kr}_{\text{xs}}$, and $r = 0.86$ when considering individual samples. Note that
 903 the GISP2 site is not included in the analysis because it is in Greenland where the elevation- $^{86}\text{Kr}_{\text{xs}}$
 904 relationship may be different from Antarctica – it does however fit the Antarctic trend rather well. We
 905 further use the simulated WAIS Divide elevation history (Golledge et al., 2014), which simulates an LGM
 906 elevation of around ~~300m~~ 300 m higher than at present at WAIS Divide.

907 **Appendix B: Sub-annual $^{86}\text{Kr}_{\text{xs}}$ variations at DE08-OH**

908 The Law Dome DE08-OH site is a revisit of the DE08 site, drilled in the 2018/2019 Austral summer
909 Antarctic field season. We have samples from two separate cores: (1) thirteen 24-cm-long samples from a
910 10-cm-diameter core going from 97 m to 193 m depth at ~ 8 m sample spacing; and (2) eight 6-cm-long
911 samples from a 24-cm-diameter core going from 97.6 m to 99.8 m depth at 30 cm sample spacing. The
912 purpose of the first set was to determine possible long-term variations in $^{86}\text{Kr}_{\text{xs}}$; the purpose of the second
913 set to assess whether there are sub-annual variations in $^{86}\text{Kr}_{\text{xs}}$ due to the seasonality in firm properties and
914 bubble trapping.

915 Both cores were dry-drilled (i.e., no drill liquid was used). The 10-cm-diameter core used was drilled at the
916 beginning of the field season, the 24-cm-diameter core at the end of the field season. Prior to shipment off
917 the continent, both cores were stored in a chest freezer at Casey Station; due to a miscommunication this
918 freezer was set to -20°C rather than -26°C , yet the ice is believed to have stayed below -18°C .

919 Both DE08-OH cores experienced more gas loss than the original DE08 core that we also sampled (Fig.
920 A1 B). In particular the samples from the 10-cm-diameter core were strongly depleted in $\delta\text{Ar}/\text{N}_2$, with the
921 most extreme gas loss seen for the deepest samples where the ice quality was poorest.

922 Fig. B1 shows the high-resolution sub-annual DE08-OH sampling. The data were corrected for gas loss and
923 thermal fractionation, using a site-mean temperature gradient of $\overline{\Delta T} = -1.6^{\circ}\text{C}$, possibly related to a rectifier
924 effect (Morgan et al. 2022). We find strong (5-fold) variations in $^{86}\text{Kr}_{\text{xs}}$ on sub-annual time scales. With an
925 expected annual layer thickness of around 1.3 m at this depth, it appears as though there may be an annual-
926 scale variation in $^{86}\text{Kr}_{\text{xs}}$; the data set has insufficient length to establish this firmly.

927 We refrain from interpreting the long-term variations in $^{86}\text{Kr}_{\text{xs}}$ in the 10-cm-diameter core for two reasons.
928 First, given the strong sub-annual variations seen in the high-resolution sampling, it is unavoidable that we
929 are aliasing the underlying signal in the core. Second, the 10-cm-diameter core suffers from strong gas loss
930 (depleted $\delta\text{Ar}/\text{N}_2$). We attribute this primarily to the dry drilling and imperfect sample storage conditions.
931 Perhaps the greater stresses during drilling a 10-cm core (compared to the 24-cm diameter core) result in
932 more micro-fractures and gas loss.

933 **Supplement**

934 A data supplement is available with this paper.

935 **Data availability**

936 Data are available here: <https://www.usap-dc.org/view/project/p0010037>, and via the data supplement to
937 this paper.

938 **Author contributions**

939 CB, JS, AJS and EJB designed research; SS, AS, BB, KK, DB, AJS, JDM and IO contributed
940 measurements; KK, DME, NB, RLP, RB, EM-T, PDN, DT, and VVP contributed ice core samples; CB
941 and WHGR analyzed reanalysis data; CB, AJS, and BB performed firm modelling; CB drafted the
942 manuscript with input from all authors.

943 **Competing Interests**

944 The authors declare no competing interests.

945 **Acknowledgements**

946 The idea for the Kr-86 excess proxy came out of discussions at the 2014 WAIS Divide Ice Core Science
947 Meeting held at Scripps Institution of Oceanography in La Jolla, CA. The authors want to thank John
948 Chiang, Justin Wettstein, Zanna Chase, Bob Anderson, Tyler Jones and Eric Steig for useful discussions,
949 data sharing and manuscript feedback, the NSF ice core facility (NSF-ICF, formerly the National Ice Core
950 Laboratory) for curating and distributing ice core samples, the European Centre for Medium-Range
951 Weather Forecasts (ECMWF) for making ERA-Interim reanalysis datasets publicly available, and the US
952 ice drilling program for coordinating ice core drilling in Antarctica. ~~Sample collection~~Ice drilling and field
953 ~~support~~ at Law Dome ~~and sample handling in Hobart~~ was ~~supported~~provided by the Australian Antarctic
954 Science Program, the Australian Antarctic Division and (at DE08-OH) the U.S. National Science
955 Foundation.

956 **Financial Support**

957 We gratefully acknowledge financial support from the U.S. National Science Foundation (grant numbers
958 ANT-0944343, ANT-1543267, ANT-1543229, ANT-1643716 and ANT-1643669), the New Zealand
959 Ministry of Business, Innovation and Employment (grant numbers RDF-VUW-1103, 15-VUW-131,
960 540GCT32).

961 **References**

- 962 Anderson, R.F., Ali, S., Bradtmiller, L.I., Nielsen, S.H.H., Fleisher, M.Q., Anderson, B.E. and Burckle, L.H. (2009)
 963 Wind-Driven Upwelling in the Southern Ocean and the Deglacial Rise in Atmospheric CO₂. *Science* 323, 1443-
 964 1448.
- 965 Baggenstos, D., Häberli, M., Schmitt, J., Shackleton, S.A., Birner, B., Severinghaus, J.P., Kellerhals, T. and Fischer,
 966 H. (2019) Earth's radiative imbalance from the Last Glacial Maximum to the present. *Proc. Natl. Acad. Sci. U. S.*
 967 *A.*, 201905447.
- 968 Bals-Elsholz, T.M., Atallah, E.H., Bosart, L.F., Wasula, T.A., Cempa, M.J. and Lupo, A.R. (2001) The Wintertime
 969 Southern Hemisphere Split Jet: Structure, Variability, and Evolution. *J. Clim.* 14, 4191-4215.
- 970 Battle, M.O., Severinghaus, J.P., Sofen, E.D., Plotkin, D., Orsi, A.J., Aydin, M., Montzka, S.A., Sowers, T. and Tans,
 971 P.P. (2011) Controls on the movement and composition of firn air at the West Antarctic Ice Sheet Divide. *Atmos.*
 972 *Chem. Phys.* 11, 11007-11021.
- 973 Bender, M., Sowers, T. and Lipenkov, V. (1995) ON THE CONCENTRATIONS OF O-2, N-2, AND AR IN
 974 TRAPPED GASES FROM ICE CORES. *J. Geophys. Res.* 100, 18651-18660.
- 975 Bender, M.L. (2002) Orbital tuning chronology for the Vostok climate record supported by trapped gas composition.
 976 *Earth Planet. Sci. Lett.* 204, 275-289.
- 977 Bereiter, B., Kawamura, K. and Severinghaus, J.P. (2018a) New methods for measuring atmospheric heavy noble gas
 978 isotope and elemental ratios in ice core samples. *Rapid communications in mass spectrometry* 32, 801-814.
- 979 Bereiter, B., Shackleton, S., Baggenstos, D., Kawamura, K. and Severinghaus, J. (2018b) Mean global ocean
 980 temperatures during the last glacial transition. *Nature* 553, 39.
- 981 Birner, B., Buizert, C., Wagner, T.J.W. and Severinghaus, J.P. (2018) The influence of layering and barometric
 982 pumping on firn air transport in a 2-D model. *The Cryosphere* 12, 2021-2037.
- 983 Braconnot, P., Luan, Y., Brewer, S. and Zheng, W. (2012) Impact of Earth's orbit and freshwater fluxes on Holocene
 984 climate mean seasonal cycle and ENSO characteristics. *Clim. Dyn.* 38, 1081-1092.
- 985 Broccoli, A.J., Dahl, K.A. and Stouffer, R.J. (2006) Response of the ITCZ to Northern Hemisphere cooling. *Geophys.*
 986 *Res. Lett.* 33, L01702.
- 987 Buizert, C., Cuffey, K.M., Severinghaus, J.P., Baggenstos, D., Fudge, T.J., Steig, E.J., Markle, B.R., Winstrup, M.,
 988 Rhodes, R.H., Brook, E.J., Sowers, T.A., Clow, G.D., Cheng, H., Edwards, L.R., Sigl, M., McConnell, J.R. and
 989 Taylor, K.C. (2015) The WAIS Divide deep ice core WD2014 chronology - part 1: Methane synchronization (68-
 990 31 ka BP) and the gas age-ice age difference. *Climate of the Past* 11, 153-173.
- 991 Buizert, C. and Severinghaus, J.P. (2016) Dispersion in deep polar firn driven by synoptic-scale surface pressure
 992 variability. *The Cryosphere* 10, 2099-2111.
- 993 Buizert, C., Sigl, M., Severi, M., Markle, B.R., Wettstein, J.J., McConnell, J.R., Pedro, J.B., Sodemann, H., Goto-
 994 Azuma, K., Kawamura, K., Fujita, S., Motoyama, H., Hirabayashi, M., Uemura, R., Stenni, B., Parrenin, F., He,
 995 F., Fudge, T.J. and Steig, E.J. (2018) Abrupt ice-age shifts in southern westerly winds and Antarctic climate forced
 996 from the north. *Nature* 563, 681-685.
- 997 Buizert, C., Sowers, T. and Blunier, T. (2013) Assessment of diffusive isotopic fractionation in polar firn, and
 998 application to ice core trace gas records. *Earth Planet. Sci. Lett.* 361, 110-119.
- 999 Cai, W., Santoso, A., Wang, G., Yeh, S.-W., An, S.-I., Cobb, K.M., Collins, M., Guilyardi, E., Jin, F.-F., Kug, J.-S.,
 1000 Lengaigne, M., McPhaden, M.J., Takahashi, K., Timmermann, A., Vecchi, G., Watanabe, M. and Wu, L. (2015)
 1001 ENSO and greenhouse warming. *Nature Clim. Change* 5, 849-859.
- 1002 Cane, M.A. (2005) The evolution of El Niño, past and future. *Earth Planet. Sci. Lett.* 230, 227-240.
- 1003 Ceppi, P., Hwang, Y.-T., Liu, X., Frierson, D.M.W. and Hartmann, D.L. (2013) The relationship between the ITCZ
 1004 and the Southern Hemispheric eddy-driven jet. *J. Geophys. Res.* 118, 5136-5146.
- 1005 Chase, Z., Anderson, R.F., Fleisher, M.Q. and Kubik, P.W. (2003) Accumulation of biogenic and lithogenic material
 1006 in the Pacific sector of the Southern Ocean during the past 40,000 years. *Deep Sea Research Part II: Topical Studies*
 1007 *in Oceanography* 50, 799-832.
- 1008 Cheng, H., Edwards, R.L., Sinha, A., Spötl, C., Yi, L., Chen, S., Kelly, M., Kathayat, G., Wang, X., Li, X., Kong, X.,
 1009 Wang, Y., Ning, Y. and Zhang, H. (2016) The Asian monsoon over the past 640,000 years and ice age terminations.
 1010 *Nature* 534, 640-646.
- 1011 Chiang, J.C. and Friedman, A.R. (2012) Extratropical cooling, interhemispheric thermal gradients, and tropical
 1012 climate change. *Annu. Rev. Earth Planet. Sci.* 40, 383-412.
- 1013 Chiang, J.C.H. and Bitz, C.M. (2005) Influence of high latitude ice cover on the marine Intertropical Convergence
 1014 Zone. *Clim. Dyn.* 25, 477-496.

1015 Chiang, J.C.H., Lee, S.-Y., Putnam, A.E. and Wang, X. (2014) South Pacific Split Jet, ITCZ shifts, and atmospheric
1016 North–South linkages during abrupt climate changes of the last glacial period. *Earth Planet. Sci. Lett.* 406, 233-
1017 246.

1018 Clement, A.C., Seager, R. and Cane, M.A. (2000) Suppression of El Niño during the Mid-Holocene by changes in the
1019 Earth's orbit. *Paleoceanography* 15, 731-737.

1020 Cobb, K.M., Westphal, N., Sayani, H.R., Watson, J.T., Di Lorenzo, E., Cheng, H., Edwards, R.L. and Charles, C.D.
1021 (2013) Highly Variable El Niño–Southern Oscillation Throughout the Holocene. *Science* 339, 67-70.

1022 Conroy, J.L., Overpeck, J.T., Cole, J.E., Shanahan, T.M. and Steinitz-Kannan, M. (2008) Holocene changes in eastern
1023 tropical Pacific climate inferred from a Galápagos lake sediment record. *Quat. Sci. Rev.* 27, 1166-1180.

1024 Cruz, F.W., Burns, S.J., Karmann, I., Sharp, W.D., Vuille, M., Cardoso, A.O., Ferrari, J.A., Dias, P.L.S. and Viana,
1025 O. (2005) Insolation-driven changes in atmospheric circulation over the past 116,000 years in subtropical Brazil.
1026 *Nature* 434, 63-66.

1027 Dee, D.P., Uppala, S.M., Simmons, A.J., Berrisford, P., Poli, P., Kobayashi, S., Andrae, U., Balmaseda, M.A.,
1028 Balsamo, G., Bauer, P., Bechtold, P., Beljaars, A.C.M., van de Berg, L., Bidlot, J., Bormann, N., Delsol, C.,
1029 Dragani, R., Fuentes, M., Geer, A.J., Haimberger, L., Healy, S.B., Hersbach, H., Hólm, E.V., Isaksen, I., Kållberg,
1030 P., Köhler, M., Matricardi, M., McNally, A.P., Monge-Sanz, B.M., Morcrette, J.J., Park, B.K., Peubey, C., de
1031 Rosnay, P., Tavolato, C., Thépaut, J.N. and Vitart, F. (2011) The ERA-Interim reanalysis: configuration and
1032 performance of the data assimilation system. *Quarterly Journal of the Royal Meteorological Society* 137, 553-597.

1033 Driscoll, R., Elliot, M., Russon, T., Welsh, K., Yokoyama, Y. and Tudhope, A. (2014) ENSO reconstructions over the
1034 past 60 ka using giant clams (*Tridacna* sp.) from Papua New Guinea. *Geophys. Res. Lett.* 41, 6819-6825.

1035 Dykoski, C.A., Edwards, R.L., Cheng, H., Yuan, D.X., Cai, Y.J., Zhang, M.L., Lin, Y.S., Qing, J.M., An, Z.S. and
1036 Revenaugh, J. (2005) A high-resolution, absolute-dated Holocene and deglacial Asian monsoon record from
1037 Dongge Cave, China. *Earth Planet. Sci. Lett.* 233, 71-86.

1038 Emile-Geay, J., Cobb, K.M., Carré, M., Braconnot, P., Leloup, J., Zhou, Y., Harrison, S.P., Corrège, T., McGregor,
1039 H.V., Collins, M., Driscoll, R., Elliot, M., Schneider, B. and Tudhope, A. (2015) Links between tropical Pacific
1040 seasonal, interannual and orbital variability during the Holocene. *Nat. Geosci.* 9, 168.

1041 Etheridge, D.M., Pearman, G.I. and Fraser, P.J. (1992) CHANGES IN TROPOSPHERIC METHANE BETWEEN
1042 1841 AND 1978 FROM A HIGH ACCUMULATION-RATE ANTARCTIC ICE CORE. *Tellus* 44, 282-294.

1043 Fahnestock, M.A., Scambos, T.A., Shuman, C.A., Arthern, R.J., Winebrenner, D.P. and Kwok, R. (2000) Snow
1044 megadune fields on the East Antarctic Plateau: Extreme atmosphere-ice interaction. *Geophys. Res. Lett.* 27, 3719-
1045 3722.

1046 Fowler, A.M., Boswijk, G., Lorrey, A.M., Gergis, J., Pirie, M., McCloskey, S.P.J., Palmer, J.G. and Wunder, J. (2012)
1047 Multi-centennial tree-ring record of ENSO-related activity in New Zealand. *Nature Climate Change* 2, 172.

1048 Fujita, S., Okuyama, J., Hori, A. and Hondoh, T. (2009) Metamorphism of stratified firn at Dome Fuji, Antarctica: A
1049 mechanism for local insolation modulation of gas transport conditions during bubble close off. *J. Geophys. Res.*
1050 114.

1051 Gergis, J.L. and Fowler, A.M. (2009) A history of ENSO events since A.D. 1525: implications for future climate
1052 change. *Clim. Change* 92, 343-387.

1053 Golledge, N.R., Menviel, L., Carter, L., Fogwill, C.J., England, M.H., Cortese, G. and Levy, R.H. (2014) Antarctic
1054 contribution to meltwater pulse 1A from reduced Southern Ocean overturning. *Nat Comm.* 5, 5107.

1055 Grachev, A.M. and Severinghaus, J.P. (2003a) Determining the thermal diffusion factor for Ar-40/Ar-36 in air to aid
1056 paleoreconstruction of abrupt climate change. *J. Phys. Chem. A* 107, 4636-4642.

1057 Grachev, A.M. and Severinghaus, J.P. (2003b) Laboratory determination of thermal diffusion constants for N-
1058 29(2)/N-28(2) in air at temperatures from -60 to 0 degrees C for reconstruction of magnitudes of abrupt climate
1059 changes using the ice core fossil-air paleothermometer. *Geochim. Cosmochim. Acta* 67, 345-360.

1060 Grootes, P.M., Stuiver, M., White, J.W.C., Johnsen, S. and Jouzel, J. (1993) Comparison of oxygen isotope records
1061 from the GISP2 and GRIP Greenland ice cores. *Nature* 366, 552-554.

1062 Headly, M.A. and Severinghaus, J.P. (2007) A method to measure Kr/N-2 ratios in air bubbles trapped in ice cores
1063 and its application in reconstructing past mean ocean temperature. *J. Geophys. Res.* 112, 12.

1064 Herron, M.M. and Langway, C.C. (1980) Firn densification: An empirical model. *J. Glaciol.* 25, 373-385.

1065 Huang, B., Banzon, V.F., Freeman, E., Lawrimore, J., Liu, W., Peterson, T.C., Smith, T.M., Thorne, P.W., Woodruff,
1066 S.D. and Zhang, H.-M. (2014) Extended Reconstructed Sea Surface Temperature Version 4 (ERSST.v4). Part I:
1067 Upgrades and Intercomparisons. *J. Clim.* 28, 911-930.

1068 Huber, C., Beyerle, U., Leuenberger, M., Schwander, J., Kipfer, R., Spahni, R., Severinghaus, J.P. and Weiler, K.
1069 (2006) Evidence for molecular size dependent gas fractionation in firn air derived from noble gases, oxygen, and
1070 nitrogen measurements. *Earth Planet. Sci. Lett.* 243, 61-73.

1071 Ikeda-Fukazawa, T., Fukumizu, K., Kawamura, K., Aoki, S., Nakazawa, T. and Hondoh, T. (2005) Effects of
1072 molecular diffusion on trapped gas composition in polar ice cores. *Earth Planet. Sci. Lett.* 229, 183-192.

1073 Kanner, L.C., Burns, S.J., Cheng, H. and Edwards, R.L. (2012) High-Latitude Forcing of the South American Summer
1074 Monsoon During the Last Glacial. *Science* 335, 570-573

1075 Kawamura, K., Severinghaus, J.P., Albert, M.R., Courville, Z.R., Fahnestock, M.A., Scambos, T., Shields, E. and
1076 Shuman, C.A. (2013) Kinetic fractionation of gases by deep air convection in polar firn. *Atmos. Chem. Phys.* 13,
1077 11141-11155.

1078 Kawamura, K., Severinghaus, J.P., Ishidoya, S., Sugawara, S., Hashida, G., Motoyama, H., Fujii, Y., Aoki, S. and
1079 Nakazawa, T. (2006) Convective mixing of air in firn at four polar sites. *Earth Planet. Sci. Lett.* 244, 672-682.

1080 Kobashi, T., Severinghaus, J.P. and Barnola, J.M. (2008a) 4 +/- 1.5 degrees C abrupt warming 11,270 yr ago identified
1081 from trapped air in Greenland ice. *Earth Planet. Sci. Lett.* 268, 397-407.

1082 Kobashi, T., Severinghaus, J.P. and Kawamura, K. (2008b) Argon and nitrogen isotopes of trapped air in the GISP2
1083 ice core during the Holocene epoch (0-11,500 B.P.): Methodology and implications for gas loss processes.
1084 *Geochim. Cosmochim. Acta* 72, 4675-4686.

1085 Kohfeld, K.E., Graham, R.M., de Boer, A.M., Sime, L.C., Wolff, E.W., Le Quéré, C. and Bopp, L. (2013) Southern
1086 Hemisphere westerly wind changes during the Last Glacial Maximum: paleo-data synthesis. *Quat. Sci. Rev.* 68,
1087 76-95.

1088 Koutavas, A., deMenocal, P.B., Olive, G.C. and Lynch-Stieglitz, J. (2006) Mid-Holocene El Niño–Southern
1089 Oscillation (ENSO) attenuation revealed by individual foraminifera in eastern tropical Pacific sediments. *Geology*
1090 34, 993-996.

1091 Koutavas, A., Lynch-Stieglitz, J., Marchitto, T.M. and Sachs, J.P. (2002) El Niño-Like Pattern in Ice Age Tropical
1092 Pacific Sea Surface Temperature. *Science* 297, 226-230.

1093 Lamy, F., Chiang, J.C.H., Martínez-Méndez, G., Thierens, M., Arz, H.W., Bosmans, J., Hebbeln, D., Lambert, F.,
1094 Lembke-Jene, L. and Stuut, J.-B. (2019) Precession modulation of the South Pacific westerly wind belt over the
1095 past million years. *Proc. Natl. Acad. Sci. U. S. A.*, 201905847.

1096 Lee, S. and Kim, H.-k. (2003) The Dynamical Relationship between Subtropical and Eddy-Driven Jets. *Journal of the*
1097 *Atmospheric Sciences* 60, 1490-1503.

1098 Lee, S.Y., Chiang, J.C., Matsumoto, K. and Tokos, K.S. (2011) Southern Ocean wind response to North Atlantic
1099 cooling and the rise in atmospheric CO₂: Modeling perspective and paleoceanographic implications.
1100 *Paleoceanography* 26.

1101 Liu, Z., Kutzbach, J. and Wu, L. (2000) Modeling climate shift of El Niño variability in the Holocene. *Geophys. Res.*
1102 *Lett.* 27, 2265-2268.

1103 Liu, Z., Lu, Z., Wen, X., Otto-Bliesner, B.L., Timmermann, A. and Cobb, K.M. (2014) Evolution and forcing
1104 mechanisms of El Niño over the past 21,000 years. *Nature* 515, 550-553.

1105 Lynch-Stieglitz, J. (2017) The Atlantic Meridional Overturning Circulation and Abrupt Climate Change. *Annual*
1106 *Review of Marine Science* 9, 83-104.

1107 Mantua, N.J. and Hare, S.R. (2002) The Pacific Decadal Oscillation. *Journal of Oceanography* 58, 35-44.

1108 Marcott, S.A., Shakun, J.D., Clark, P.U. and Mix, A.C. (2013) A Reconstruction of Regional and Global Temperature
1109 for the Past 11,300 Years. *Science* 339, 1198-1201.

1110 Marino, G., Zahn, R., Ziegler, M., Purcell, C., Knorr, G., Hall, I.R., Ziveri, P. and Elderfield, H. (2013) Agulhas salt-
1111 leakage oscillations during abrupt climate changes of the Late Pleistocene. *Paleoceanography* 28, 599-606.

1112 Markle, B.R., Steig, E.J., Buizert, C., Schoenemann, S.W., Bitz, C.M., Fudge, T.J., Pedro, J.B., Ding, Q., Jones, T.R.,
1113 White, J.W.C. and Sowers, T. (2017) Global atmospheric teleconnections during Dansgaard-Oeschger events.
1114 *Nature Geosci* 10, 36-40.

1115 Marshall, J. and Speer, K. (2012) Closure of the meridional overturning circulation through Southern Ocean
1116 upwelling. *Nature Geosci* 5, 171-180.

1117 McGee, D., Donohoe, A., Marshall, J. and Ferreira, D. (2014) Changes in ITCZ location and cross-equatorial heat
1118 transport at the Last Glacial Maximum, Heinrich Stadial 1, and the mid-Holocene. *Earth Planet. Sci. Lett.* 390, 69-
1119 79.

1120 Merkel, U., Prange, M. and Schulz, M. (2010) ENSO variability and teleconnections during glacial climates. *Quat.*
1121 *Sci. Rev.* 29, 86-100.

1122 Mo, K.C. and Paegle, J.N. (2001) The Pacific–South American modes and their downstream effects. *International*
1123 *Journal of Climatology* 21, 1211-1229.

1124 Moy, C.M., Seltzer, G.O., Rodbell, D.T. and Anderson, D.M. (2002) Variability of El Niño/Southern Oscillation
1125 activity at millennial timescales during the Holocene epoch. *Nature* 420, 162.

1126 Nakamura, H. and Shimpo, A. (2004) Seasonal Variations in the Southern Hemisphere Storm Tracks and Jet Streams
1127 as Revealed in a Reanalysis Dataset. *J. Clim.* 17, 1828-1844.

1128 Orsi, A.J., Kawamura, K., Fegyveresi, J.M., Headly, M.A., Alley, R.B. and Severinghaus, J.P. (2015) Differentiating
1129 bubble-free layers from melt layers in ice cores using noble gases. *J. Glaciol.* 61, 585-594.

1130 Oyabu, I., Kawamura, K., Uchida, T., Fujita, S., Kitamura, K., Hirabayashi, M., Aoki, S., Morimoto, S., Nakazawa,
1131 T., Severinghaus, J.P. and Morgan, J.D. (2021) Fractionation of O₂N₂ and ArN₂ in the Antarctic ice sheet during
1132 bubble formation and bubble-clathrate hydrate transition from precise gas measurements of the Dome Fuji ice
1133 core. *The Cryosphere* 15, 5529-5555.

1134 Parkinson, C.L. and Cavalieri, D.J. (2012) Antarctic sea ice variability and trends, 1979–2010. *The Cryosphere*
1135 6, 871-880.

1136 Pedro, J.B., Jochum, M., Buizert, C., He, F., Barker, S. and Rasmussen, S.O. (2018) Beyond the bipolar seesaw:
1137 Toward a process understanding of interhemispheric coupling. *Quat. Sci. Rev.* 192, 27-46.

1138 Peterson, L.C., Haug, G.H., Hughen, K.A. and Röhl, U. (2000) Rapid Changes in the Hydrologic Cycle of the Tropical
1139 Atlantic During the Last Glacial. *Science* 290, 1947-1951.

1140 Rahmstorf, S. (2002) Ocean circulation and climate during the past 120,000 years. *Nature* 419, 207-214.

1141 Raynaud, D., Lipenkov, V., Lemieux-Dudon, B., Duval, P., Loutre, M.F. and Lhomme, N. (2007) The local insolation
1142 signature of air content in Antarctic ice. A new step toward an absolute dating of ice records. *Earth Planet. Sci.*
1143 *Lett.* 261, 337-349.

1144 Rein, B., Lückge, A., Reinhardt, L., Sirocko, F., Wolf, A. and Dullo, W.-C. (2005) El Niño variability off Peru during
1145 the last 20,000 years. *Paleoceanography* 20.

1146 Rhodes, R.H., Faïn, X., Brook, E.J., McConnell, J.R., Maselli, O.J., Sigl, M., Edwards, J., Buizert, C., Blunier, T.,
1147 Chappellaz, J. and Freitag, J. (2016) Local artifacts in ice core methane records caused by layered bubble trapping
1148 and in situ production: a multi-site investigation. *Clim. Past* 12, 1061-1077.

1149 Riedinger, M.A., Steinitz-Kannan, M., Last, W.M. and Brenner, M. (2002) A ~6100 14C yr record of El Niño activity
1150 from the Galápagos Islands. *Journal of Paleolimnology* 27, 1-7.

1151 Rind, D., Russell, G., Schmidt, G., Sheth, S., Collins, D., Demenocal, P. and Teller, J. (2001) Effects of glacial
1152 meltwater in the GISS coupled atmosphere-ocean model: 2. A bipolar seesaw in Atlantic Deep Water production.
1153 *Journal of Geophysical Research: Atmospheres* (1984–2012) 106, 27355-27365.

1154 Rojas, M., Moreno, P., Kageyama, M., Crucifix, M., Hewitt, C., Abe-Ouchi, A., Ohgaito, R., Brady, E.C. and Hope,
1155 P. (2009) The Southern Westerlies during the last glacial maximum in PMIP2 simulations. *Clim. Dyn.* 32, 525-
1156 548.

1157 Russell, J.L., Dixon, K.W., Gnanadesikan, A., Stouffer, R.J. and Toggweiler, J.R. (2006) The Southern Hemisphere
1158 Westerlies in a Warming World: Propping Open the Door to the Deep Ocean. *J. Clim.* 19, 6382-6390.

1159 Sadekov, A.Y., Ganeshram, R., Pichevin, L., Berdin, R., McClymont, E., Elderfield, H. and Tudhope, A.W. (2013)
1160 Palaeoclimate reconstructions reveal a strong link between El Niño-Southern Oscillation and Tropical Pacific mean
1161 state. *Nature Communications* 4, 2692.

1162 Salau, O., Schneider, B., Park, W., Khon, V. and Latif, M. (2012) Modeling the ENSO impact of orbitally induced
1163 mean state climate changes. *J. Geophys. Res.* 117.

1164 Schaller, C.F., Freitag, J. and Eisen, O. (2017) Critical porosity of gas enclosure in polar firn independent of climate.
1165 *Clim. Past* 13, 1685-1693.

1166 Schneider, T., Bischoff, T. and Haug, G.H. (2014) Migrations and dynamics of the intertropical convergence zone.
1167 *Nature* 513, 45-53.

1168 Schwander, J. (1989) The transformation of snow to ice and the occlusion of gases in: Oescher, H., Langway, C.C.
1169 (Eds.), *The Environmental record in glaciers and ice sheets*. John Wiley, New York, pp. 53-67.

1170 Schwander, J., Barnola, J.M., Andrie, C., Leuenberger, M., Ludin, A., Raynaud, D. and Stauffer, B. (1993) THE AGE
1171 OF THE AIR IN THE FIRN AND THE ICE AT SUMMIT, GREENLAND. *J. Geophys. Res.* 98, 2831-2838.

1172 Schwander, J., Stauffer, B. and Sigg, A. (1988) Air mixing in firn and the age of the air at pore close-off, *Annals of*
1173 *Glaciology*, pp. 141-145.

1174 Severinghaus, J.P., Albert, M.R., Courville, Z.R., Fahnestock, M.A., Kawamura, K., Montzka, S.A., Muhle, J.,
1175 Scambos, T.A., Shields, E., Shuman, C.A., Suwa, M., Tans, P. and Weiss, R.F. (2010) Deep air convection in the
1176 firn at a zero-accumulation site, central Antarctica. *Earth Planet. Sci. Lett.* 293, 359-367.

1177 Severinghaus, J.P. and Battle, M.O. (2006) Fractionation of gases in polar ice during bubble close-off: New constraints
1178 from firn air Ne, Kr and Xe observations. *Earth Planet. Sci. Lett.* 244, 474-500.

1179 Severinghaus, J.P., Beaudette, R., Headly, M.A., Taylor, K. and Brook, E.J. (2009) Oxygen-18 of O₂ Records the
1180 Impact of Abrupt Climate Change on the Terrestrial Biosphere. *Science* 324, 1431-1434.

1181 Severinghaus, J.P., Grachev, A., Luz, B. and Caillon, N. (2003) A method for precise measurement of argon 40/36
1182 and krypton/argon ratios in trapped air in polar ice with applications to past firn thickness and abrupt climate
1183 change in Greenland and at Siple Dome, Antarctica. *Geochim. Cosmochim. Acta* 67, 325-343.

1184 Severinghaus, J.P., Sowers, T., Brook, E.J., Alley, R.B. and Bender, M.L. (1998) Timing of abrupt climate change at
1185 the end of the Younger Dryas interval from thermally fractionated gases in polar ice. *Nature* 391, 141-146.

1186 Shakun, J.D., Clark, P.U., He, F., Marcott, S.A., Mix, A.C., Liu, Z., Otto-Bliesner, B., Schmittner, A. and Bard, E.
1187 (2012) Global warming preceded by increasing carbon dioxide concentrations during the last deglaciation. *Nature*
1188 484, 49-54.

1189 Sime, L.C., Kohfeld, K.E., Le Quéré, C., Wolff, E.W., de Boer, A.M., Graham, R.M. and Bopp, L. (2013) Southern
1190 Hemisphere westerly wind changes during the Last Glacial Maximum: model-data comparison. *Quat. Sci. Rev.*
1191 64, 104-120.

1192 Simpson, I.R., Hitchcock, P., Shepherd, T.G. and Scinocca, J.F. (2011) Stratospheric variability and tropospheric
1193 annular-mode timescales. *Geophys. Res. Lett.* 38.

1194 Sowers, T., Bender, M., Raynaud, D. and Korotkevich, Y.S. (1992) $\delta^{15}\text{N}$ of N_2 in air trapped in polar ice: A tracer
1195 of gas transport in the firn and a possible constraint on ice age-gas age differences. *J. Geophys. Res.* 97, 15683-
1196 15697.

1197 Stott, L., Poulsen, C., Lund, S. and Thunell, R. (2002) Super ENSO and Global Climate Oscillations at Millennial
1198 Time Scales. *Science* 297, 222-226.

1199 Studer, A.S., Sigman, D.M., Martínez-García, A., Benz, V., Winckler, G., Kuhn, G., Esper, O., Lamy, F., Jaccard,
1200 S.L., Wacker, L., Oleynik, S., Gersonde, R. and Haug, G.H. (2015) Antarctic Zone nutrient conditions during the
1201 last two glacial cycles. *Paleoceanography* 30, 2014PA002745.

1202 Studer, A.S., Sigman, D.M., Martínez-García, A., Thöle, L.M., Michel, E., Jaccard, S.L., Lippold, J.A., Mazaud, A.,
1203 Wang, X.T., Robinson, L.F., Adkins, J.F. and Haug, G.H. (2018) Increased nutrient supply to the Southern Ocean
1204 during the Holocene and its implications for the pre-industrial atmospheric CO_2 rise. *Nat. Geosci.* 11, 756-760.

1205 Thomas, E.R., Marshall, G.J. and McConnell, J.R. (2008) A doubling in snow accumulation in the western Antarctic
1206 Peninsula since 1850. *Geophys. Res. Lett.* 35.

1207 Thompson, D.W.J. and Wallace, J.M. (2000) Annular Modes in the Extratropical Circulation. Part I: Month-to-Month
1208 Variability*. *J. Clim.* 13, 1000-1016.

1209 Thompson, L.G., Mosley-Thompson, E., Davis, M.E., Zagorodnov, V.S., Howat, I.M., Mikhalevko, V.N. and Lin, P.-
1210 N. (2013) Annually Resolved Ice Core Records of Tropical Climate Variability over the Past ~1800 Years. *Science*
1211 340, 945-950.

1212 Timmermann, A., Okumura, Y., An, S.I., Clement, A., Dong, B., Guilyardi, E., Hu, A., Jungclauss, J.H., Renold, M.,
1213 Stocker, T.F., Stouffer, R.J., Sutton, R., Xie, S.P. and Yin, J. (2007) The Influence of a Weakening of the Atlantic
1214 Meridional Overturning Circulation on ENSO. *J. Clim.* 20, 4899-4919.

1215 Toggweiler, J.R., Russell, J.L. and Carson, S.R. (2006) Midlatitude westerlies, atmospheric CO_2 , and climate change
1216 during the ice ages. *Paleoceanography* 21, PA2005.

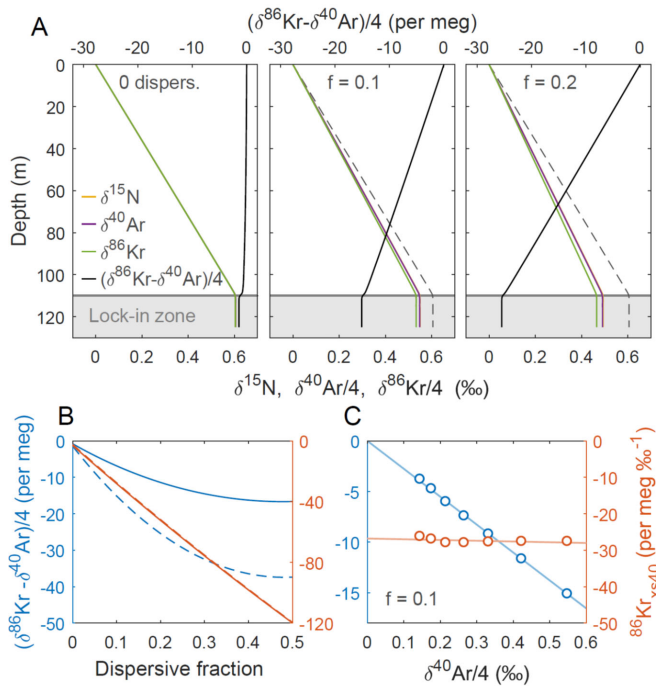
1217 Trenberth, K.E. (1991) Storm Tracks in the Southern Hemisphere. *Journal of the Atmospheric Sciences* 48, 2159-
1218 2178.

1219 Tudhope, A.W., Chilcott, C.P., McCulloch, M.T., Cook, E.R., Chappell, J., Ellam, R.M., Lea, D.W., Lough, J.M. and
1220 Shimmield, G.B. (2001) Variability in the El Niño-Southern Oscillation through a glacial-interglacial cycle.
1221 *Science* 291, 1511-1517.

1222 Wang, X., Auler, A.S., Edwards, R.L., Cheng, H., Ito, E., Wang, Y., Kong, X. and Solheid, M. (2007) Millennial-
1223 scale precipitation changes in southern Brazil over the past 90,000 years. *Geophys. Res. Lett.* 34.

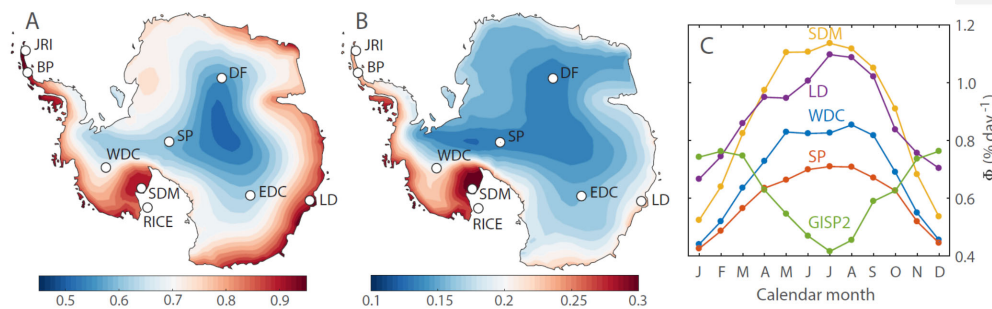
1224 Wang, Y.J., Cheng, H., Edwards, R.L., An, Z.S., Wu, J.Y., Shen, C.C. and Dorale, J.A. (2001) A High-Resolution
1225 Absolute-Dated Late Pleistocene Monsoon Record from Hulu Cave, China. *Science* 294, 2345-2348.

1226 Zheng, W., Braconnot, P., Guilyardi, E., Merkel, U. and Yu, Y. (2008) ENSO at 6ka and 21ka from ocean-atmosphere
1227 coupled model simulations. *Clim. Dyn.* 30, 745-762.



1228

1229 **Figure 1.** Idealized firn air transport model experiments of $^{86}\text{Kr}_{\text{xs}}$. Firn density is calculated using (Herron
 1230 and Langway, 1980), and the diffusivity using (Schwander, 1989). **A** Simulations using a fraction of
 1231 dispersive mixing of $f=0$ (left), $f=0.1$ (middle) and $f=0.2$ (right) for a hypothetical site with accumulation
 1232 rate of $A = 2 \text{ cm a}^{-1}$ ice equivalent and mean annual temperature $T = -60^\circ\text{C}$. At dispersive fraction f , effective
 1233 molecular diffusivity of all gases is multiplied by $(1-f)$ and dispersive mixing for all gases is set equal to f
 1234 times the effective molecular diffusivity of CO_2 . **B** Isotopic disequilibrium as a function of dispersive
 1235 mixing intensity at two different firn thicknesses of around 100 m (dashed, $A = 2 \text{ cm a}^{-1}$ and $T = -60^\circ\text{C}$) and
 1236 50 m (solid, $A = 2 \text{ cm a}^{-1}$ and $T = -43^\circ\text{C}$). We compare isotopic disequilibrium without (blue, left axis) and
 1237 with (orange, right axis) normalization. **C** Simulations at 10 % dispersive mixing, where each dot represents
 1238 different climatic conditions. Accumulation rate is $A = 2 \text{ cm a}^{-1}$ ice equivalent and mean annual temperature
 1239 is changed from -60°C to -30°C in steps of 5°C .



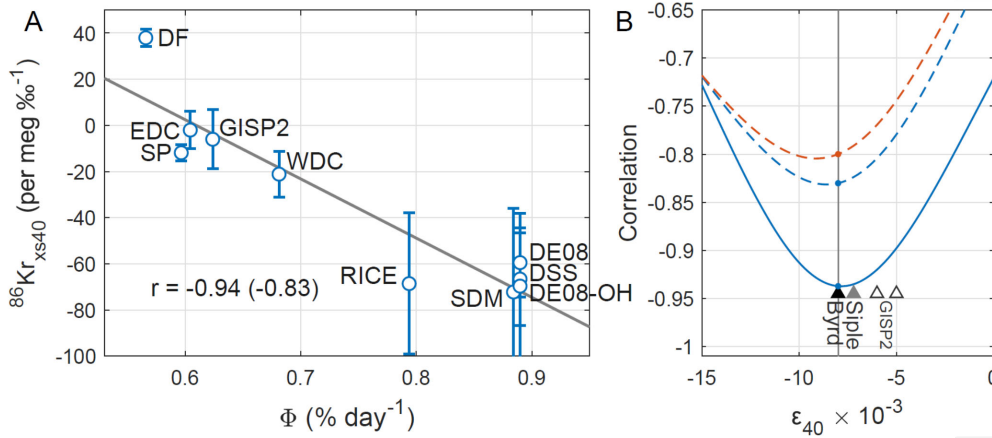
1240

1241

1242 **Figure 2.** Calibrating Kr-86 excess. **A** Annual-mean Φ in Antarctica over 1979-2017, in units of $\% \text{ day}^{-1}$.

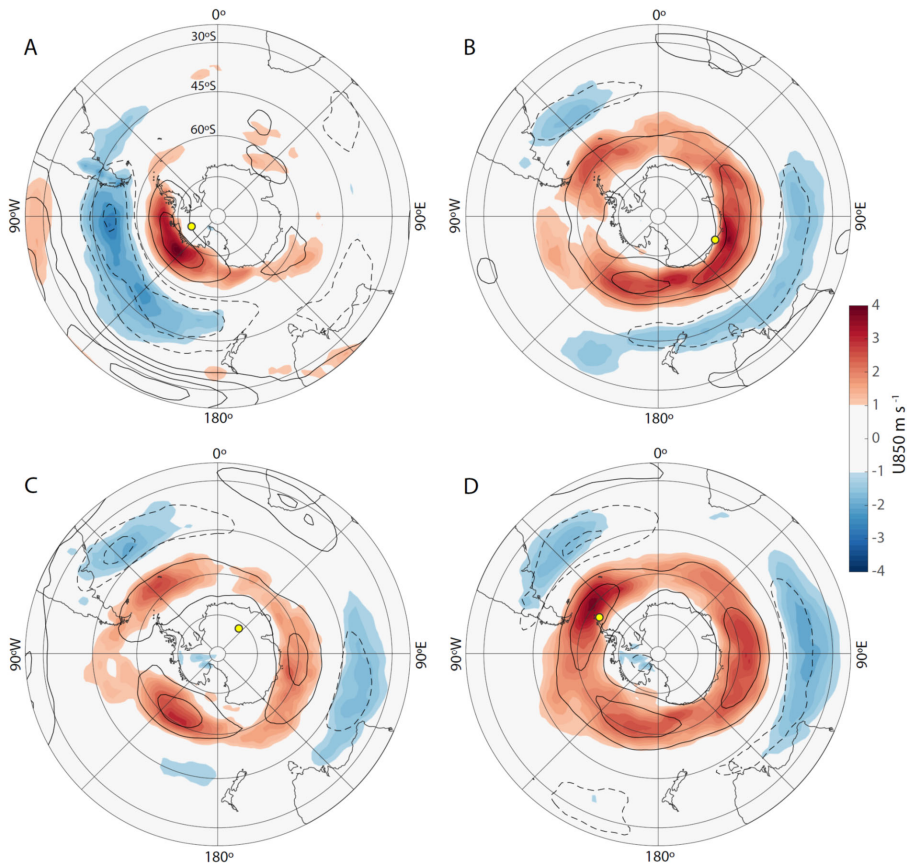
1243 **B** Interannual variability (1σ standard deviation) of annual-mean Φ over 1979-2017, in units of $\% \text{ day}^{-1}$. **C**

1244 Annual cycle in Φ for 1979-2017 for the indicated sites.



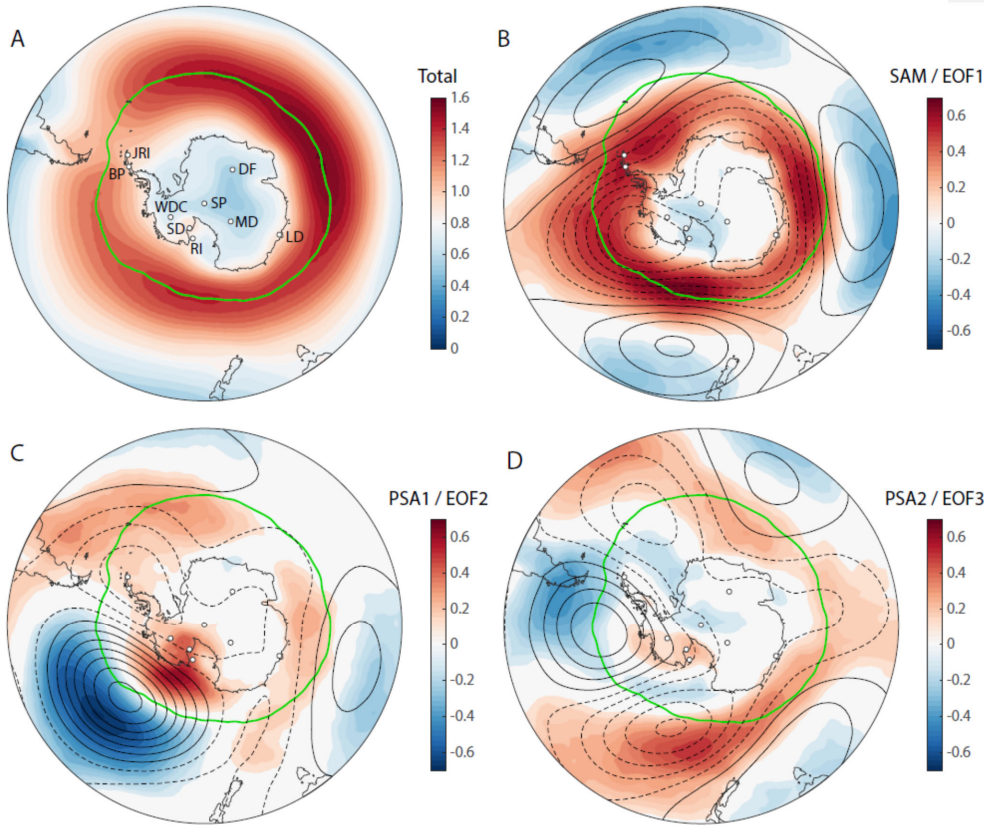
1245

1246 **Figure 3.** Calibrating Kr-86 excess. **A** $^{86}\text{Kr}_{\text{xs}}$ as a function of Φ for the calibration data set. Circles give the
 1247 site mean, and the error bars denote the $\pm 1\sigma$ standard deviation between samples (uncertainty in corrections
 1248 and measurements not included). The number of samples at each site is given in Table 1. Pearson correlation
 1249 coefficient is $r = -0.94$ when considering site data means and $r = -0.83$ when considering all individual
 1250 samples. Data are corrected for gas loss using $\epsilon_{40} = -0.008$ (Appendix A1), and corrected for thermal
 1251 fractionation using site-mean N-15 excess (Appendix A2). The calibration curve for $^{86}\text{Kr}_{\text{xs}15}$ is identical in
 1252 this case, with slightly larger errorbars. **B** Correlation of the calibration curve as a function of the gas loss
 1253 correction scaling parameter ϵ_{40} . The solid line gives the correlation for both site-mean $^{86}\text{Kr}_{\text{xs}15}$ and $^{86}\text{Kr}_{\text{xs}40}$
 1254 (identical); the dashed lines the correlation using individual samples for $^{86}\text{Kr}_{\text{xs}40}$ (blue) and $^{86}\text{Kr}_{\text{xs}15}$ (orange).
 1255 Triangles denote the ϵ_{40} estimate from the Byrd, Siple and GISP2 ice cores (Fig. A2; Kobashi et al., 2008a;
 1256 Severinghaus et al., 2003).



1257

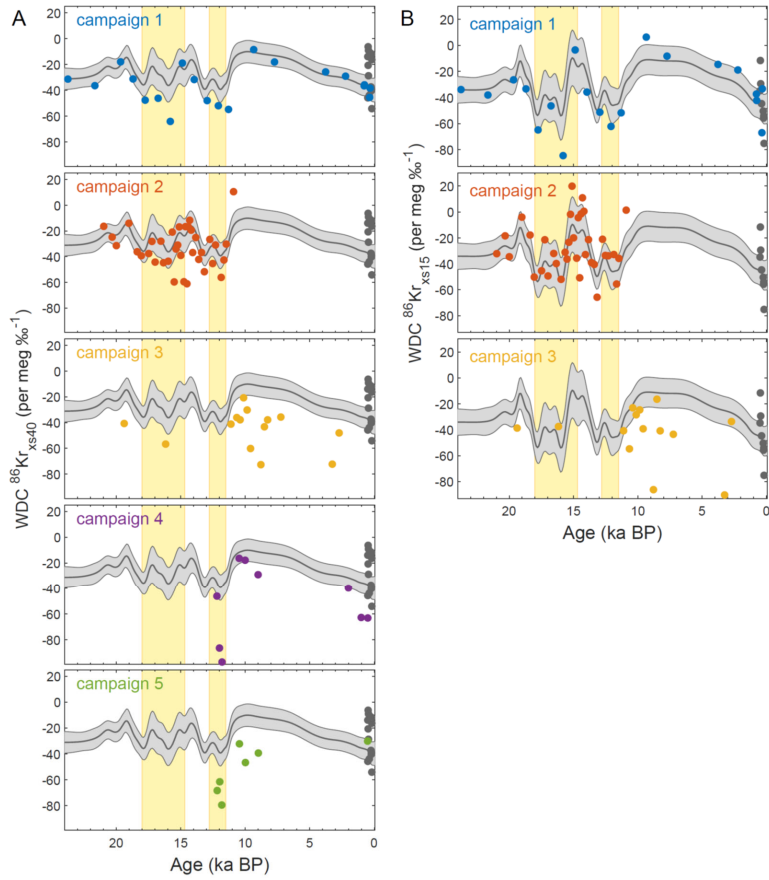
1258 **Figure 4.** Zonal wind speed at 850 hPa (color shading, see scale bar) and 200 hPa (2 m s^{-1} contours)
 1259 regressed onto surface synoptic activity Φ at the Antarctic ice core sites of: **A** WAIS Divide; **B** Law
 1260 Dome (DE08, DE08-OH and DSSW20K); **C** Dome Fuji; **D** James Ross Island. Yellow dots mark the ice
 1261 core locations.



1262

1263 **Figure 5.** Modes of SH extratropical atmospheric variability and their link to synoptic-scale surface
 1264 pressure variability in Antarctica. **A** Annual mean Φ in units of $\% \text{ day}^{-1}$; latitude of maximum Φ denoted
 1265 by green line. **B** Colors show correlation between Φ and the Southern Annular Mode (SAM) index, with
 1266 superimposed the 500 hPa geopotential height anomalies in 10 m contours- (positive contours solid,
 1267 negative contours dashed). **C** as panel B, but for the Pacific-South American Pattern 1 (PSA1). **D** As panel
 1268 B, but for the Pacific-South American Pattern 2 (PSA2). SAM, PSA1 and PSA2 are defined as respectively
 1269 the first, second and third EOFs (Empirical Orthogonal Functions) of the 500 hPa geopotential height
 1270 anomalies in 20° - 90° S monthly values in the 1979-2017 ERA interim reanalysis (Dee et al., 2011). In all
 1271 panels the latitude of maximum Φ is denoted by the green line.

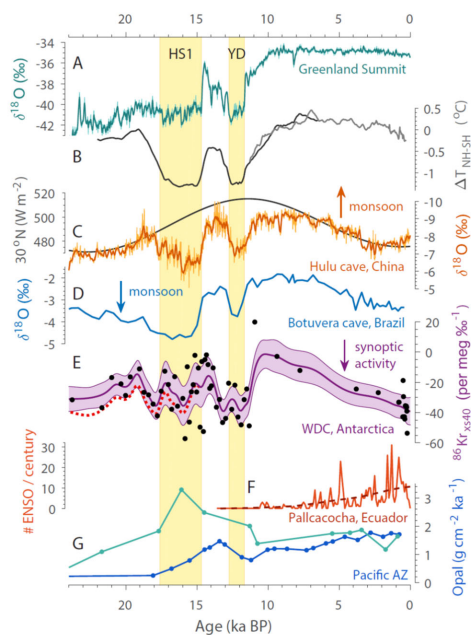
1272



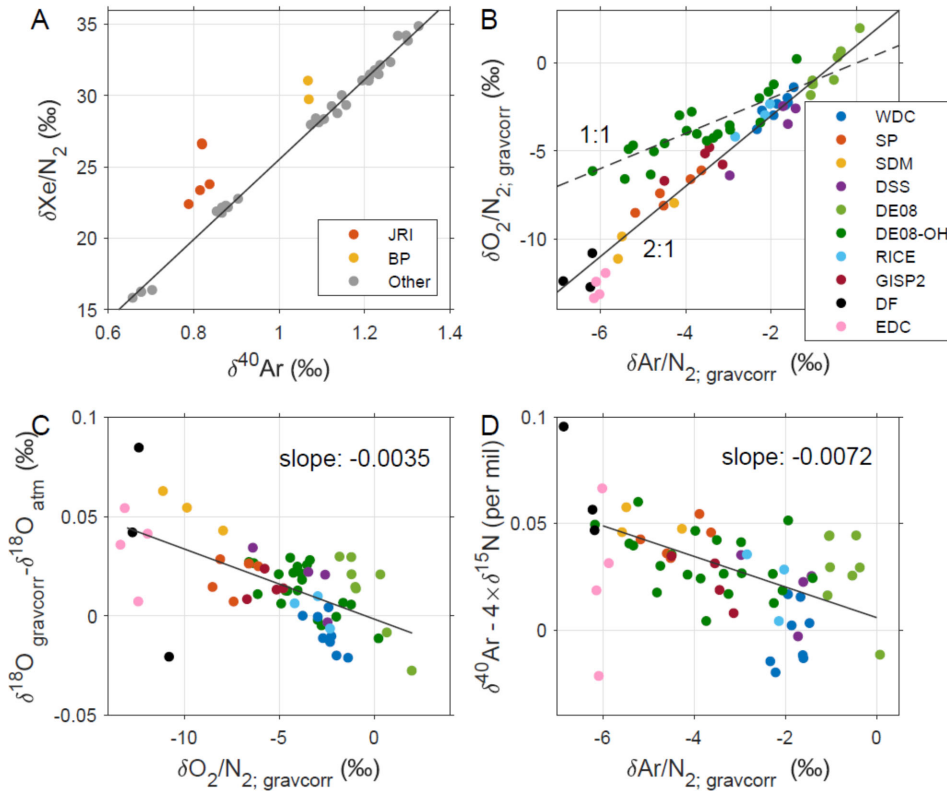
1273

1274

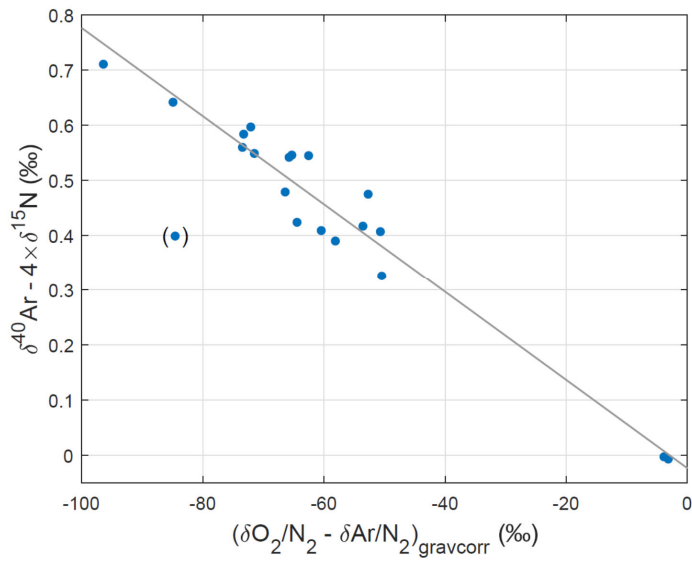
1275 **Figure 6.** WAIS Divide Kr-86 excess records through the last deglaciation. **A** WDC $^{86}\text{Kr}_{\text{xs40}}$ data from the
1276 five measurement campaigns. The gray curve shows a Gaussian smoothing curve to the combined data
1277 from the first two campaigns; the light gray shaded area shows the $\pm 1\sigma$ uncertainty envelope based on a
1278 10,000 iteration Monte-Carlo sampling of the errors and uncertainties. The WDC calibration data is shown
1279 as gray circles for comparison. **B** As in panel (A), but for $^{86}\text{Kr}_{\text{xs15}}$. For campaigns 4 and 5 the sample was
1280 not split, and no $\delta^{15}\text{N}$ data are available. The Heinrich Stadial 1 and Younger Dryas North-Atlantic cold
1281 periods marked in yellow. Thermal corrections in the WDC $^{86}\text{Kr}_{\text{xs}}$ records are based on firm model
1282 simulations.



1285 **Figure 7.** Climate records through the last deglaciation with the Heinrich Stadial 1 (HS1) and Younger
 1286 Dryas (YD) North-Atlantic cold periods marked in yellow. **A** Greenland Summit ice core stable water
 1287 isotope ratio $\delta^{18}\text{O}$ here the average of the GISP2 and GRIP ice cores (Grootes et al., 1993). **B** Hemispheric
 1288 temperature difference (McGee et al., 2014) based on global proxy compilations for the Holocene (Marcott
 1289 et al., 2013) and last deglaciation (Shakun et al., 2012). **C** Speleothem calcite $\delta^{18}\text{O}$ from Hulu and Dongge
 1290 Caves, China, as a proxy for East Asian summer monsoon strength (Dykoski et al., 2005; Wang et al.,
 1291 2001). Superimposed is summer solstice (June 21) insolation at 30°N . **D** Speleothem calcite $\delta^{18}\text{O}$ from
 1292 Botuvera cave, southern Brazil, as a proxy for South American summer monsoon strength (Cruz et al.,
 1293 2005; Wang et al., 2007). **E** Kr-86 excess record from WAIS Divide (this study); corrected for gas loss and
 1294 thermal fractionation (Appendix A). Center line and shaded envelope show the mean and $\pm 1\sigma$ uncertainty
 1295 interval of a 10,000 iteration Monte Carlo smoothing exercise (see text). The dotted red line equals the
 1296 center line with a correction for elevation change applied (Appendix A) using a simulated elevation history
 1297 (Golledge et al., 2014). **F** Number of El Niño events per century from laminations in sediments from Laguna
 1298 Pallacocha, Ecuador (Moy et al., 2002). **G** Th-normalized opal flux in the Pacific Antarctic zone (south of
 1299 the polar front) from cores NBP9802-6PC1 (turquoise; 169.98°W , 61.88°S) and PS75/072-4 (blue;
 1300 151.22°W , 57.56°S), reflecting local productivity and (wind-driven) upwelling (Chase et al., 2003; Studer
 1301 et al., 2015). All isotope data in this figure are on the V-SMOW scale. Arrows show direction of increased
 1302 monsoon strength / synoptic activity.



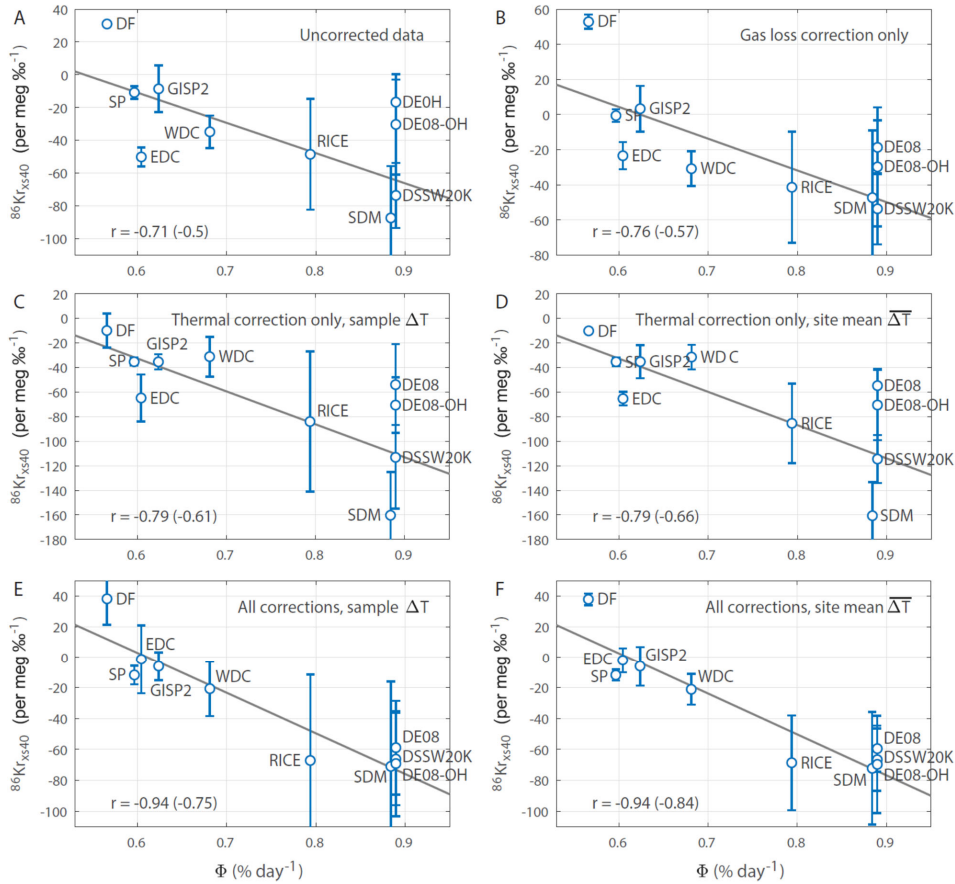
1303
 1304 **Figure A1.** Elemental ratios in the 11-site calibration study of late Holocene samples. **A** $\delta\text{Xe}/\text{N}_2$ vs. $\delta^{40}\text{Ar}$
 1305 in all ice core samples. $\delta^{40}\text{Ar}$ is used solely to illustrate gravitational enrichment, and a similar picture arises
 1306 when plotted against any isotopic pair. Refrozen meltwater (elevated $\delta\text{Xe}/\text{N}_2$) was seen in all samples from
 1307 the Antarctic Peninsula (James Ross Island and Bruce Plateau sites), despite selecting samples free of
 1308 visible melt features. **B** The relationship between the commonly used gas loss proxies $\delta\text{O}_2/\text{N}_2$ and $\delta\text{Ar}/\text{N}_2$
 1309 corrected for gravity. **C** Enrichment in $\delta^{18}\text{O}$ (corrected for gravity and atmospheric $\delta^{18}\text{O}_{\text{atm}}$) plotted against
 1310 gravity-corrected $\delta\text{O}_2/\text{N}_2$ **D** $\delta^{40}\text{Ar}$ enrichment plotted against gravity-corrected $\delta\text{Ar}/\text{N}_2$. In all panels
 1311 gravitational correction is applied by subtracting $\delta^{15}\text{N}$ times the atomic mass unit difference.



1312

1313 **Figure A2.** Argon isotopic enrichment due to gas loss in the Byrd core used to determine the $\delta^{40}\text{Ar}$ gas
 1314 loss correction (appendix A1). The enrichment in $\delta^{40}\text{Ar}$ plotted as a function of gravitationally corrected
 1315 $(\delta\text{O}_2/\text{N}_2 - \delta\text{Ar}/\text{N}_2)_{\text{gravcorr}}$ measured in the deep Antarctic Byrd ice core, which suffered heavy gas loss. Ice samples
 1316 were analyzed in the Bender Lab at the University of Rhode Island by Jeff Severinghaus in 1997. The slope
 1317 of the least-square fit is $\epsilon_{40} = -0.008$. The data point in parentheses is treated as an outlier and excluded
 1318 from the fitting.

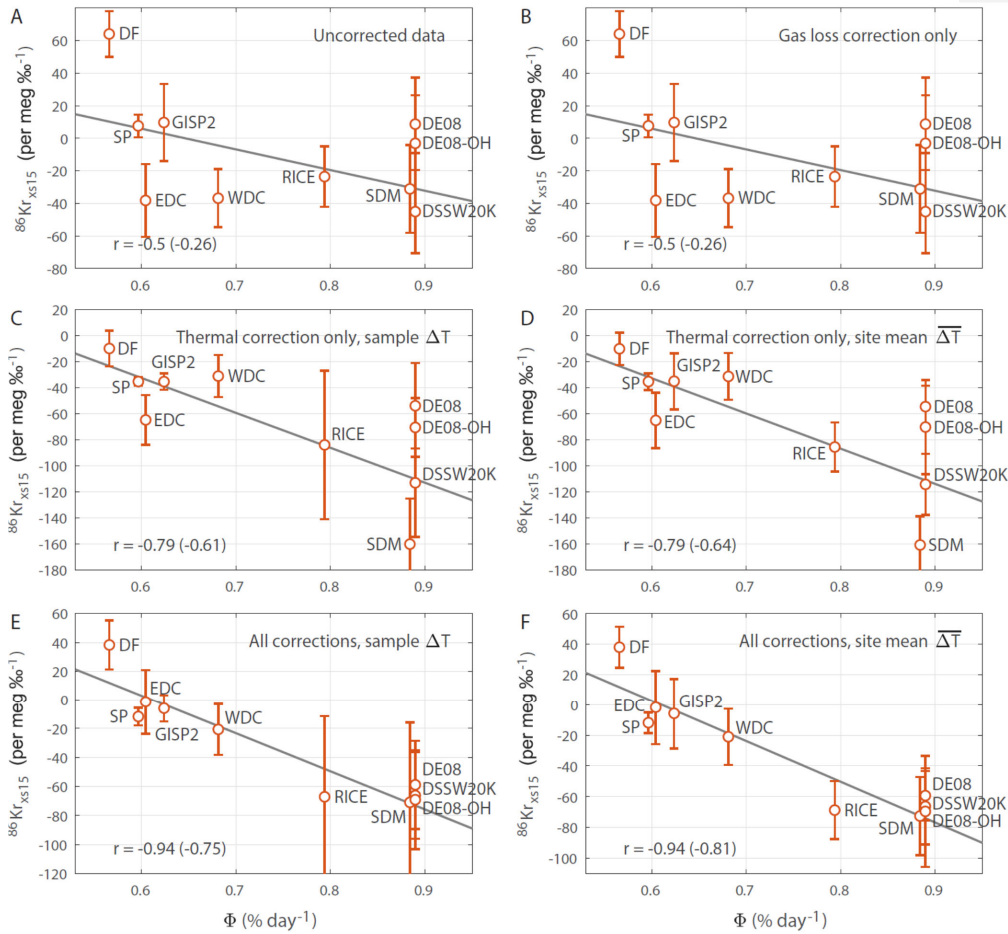
1319



1320

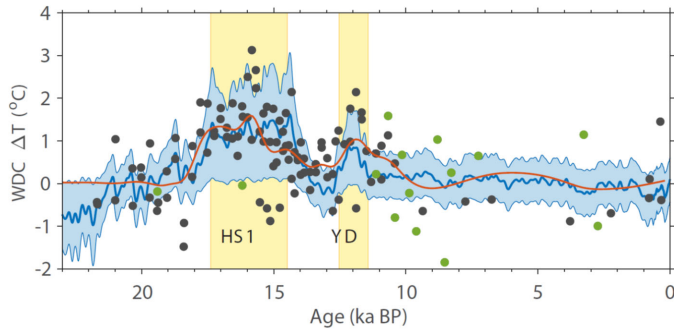
1321

1322 **Figure A3.** Influence of gas loss and thermal correction on the $^{86}\text{Kr}_{\text{xs40}}$ calibration. We plot $^{86}\text{Kr}_{\text{xs40}}$ as a
 1323 function of Φ A without any data corrections applied; **B** with only the gas loss correction applied ($\epsilon_{40} = -$
 1324 0.008); **C** with only the thermal correction applied using individual sample ΔT ; **D** with only the thermal
 1325 correction applied using individual site mean $\overline{\Delta T}$; **E** with both gas loss and thermal corrections applied
 1326 using individual sample ΔT ; **F** with both gas loss and thermal corrections applied using site mean $\overline{\Delta T}$. In
 1327 each panel the correlation to Φ are listed for the site-average and individual sample with the latter in
 1328 parentheses. For all correlations $p < 0.05$.

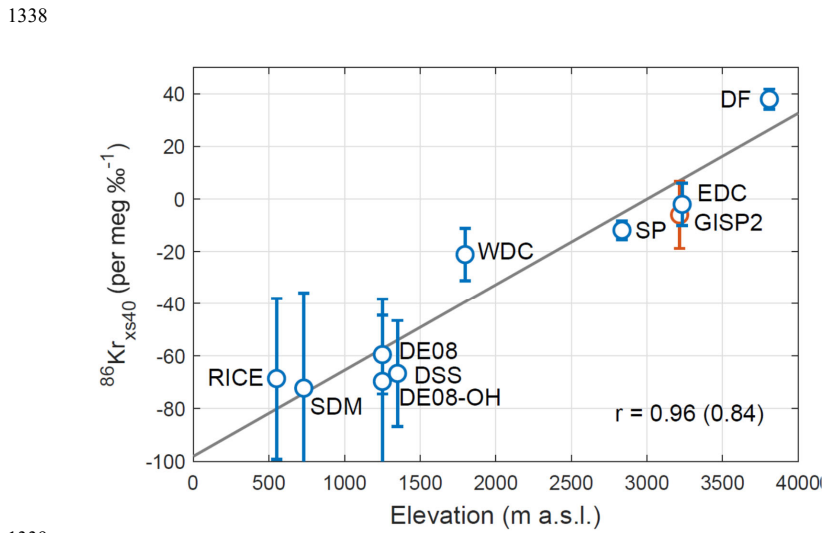


1329

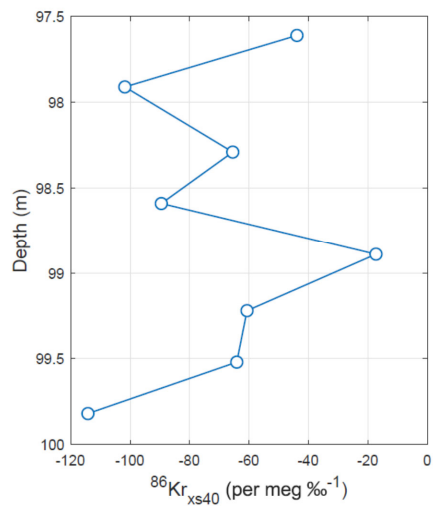
1330 **Figure A4.** Same as figure A3, but for $^{86}\text{Kr}_{\text{xs15}}$. Note that the gas loss correction (panel B) does not impact
 1331 $^{86}\text{Kr}_{\text{xs15}}$. For all correlations $p < 0.05$, except for panels A and B where $p = 0.16$ for the site-average
 1332 correlation.



1333
 1334 **Figure A5.** The ΔT correction applied to the downcore records. Blue envelope shows the $\pm 2\sigma$ range of
 1335 thermal correction scenarios in the Monte Carlo sampling, together with the mean (blue line). Gray dots
 1336 show WDC ΔT estimates from available ^{15}N -excess data, with the red curve being a Gaussian smoothing
 1337 function to the data. Green dots are ^{15}N -excess from campaign 3, showing somewhat greater scatter.



1339
 1340 **Figure A6.** Kr-86 excess dependence on site elevation. Vertical axis is the $^{86}\text{Kr}_{\text{xs}}$. The linear fit has a slope
 1341 of 34 per meg $\%^{-1}$ per 1000 m elevation.



1342

1343 **Figure B1** High-resolution sub-annual sampling of $^{86}\text{Kr}_{\text{xs40}}$ in the DE08-OH site. The annual layer thickness
 1344 at this depth is around 1.3 m.

1345 **Table 1.** Ice core sites used in this study, with N the number of samples included in the calibration study.
 1346 See the main text for acronyms.
 1347

Site	T (°C)	A (m ice a ⁻¹)	Φ (% day ⁻¹)	Latitude	Longitude	N
WDC	-31	0.22	0.68	79.5°S	112.1°W	8 ^a
DF	-57	0.028	0.56	77.3°S	39.7°E	3
SP	-51	0.078	0.6	90.0°S	98.2°W	5
SDM	-25	0.13	0.88	81.7°S	149.1°W	3
DSSW20K	-21	0.16	0.89	66.8°S	112.6°E	4
DE08	-19	1.2	0.89	66.7°S	113.2°E	8
DE08-OH	-19	1.2	0.89	66.7°S	113.2°E	8 ^b
RICE	-24	0.24	0.79	79.4°S	161.7°W	3 ^a
EDC	-55	0.03	0.6	75.1°S	123.4°E	4
JRI	-14	0.68	0.97	64.2°S	57.7°W	5 ^c
BPBRP	-15	2	0.9	66.1°S	64.1°W	2 ^c
GISP2	-32	0.23	0.62	72.6°N	38.5°W	4

1348 ^aNot including one sample rejected due to technical problems.

1349 ^bOnly shallow samples due to strong gas loss in deeper samples attributed to warm storage conditions.

1350 ^cRefrozen meltwater present as indicated by elevated Xe/N₂ ratio.
 1351
 1352
 1353
 1354

1355 **Table 2.** Pearson correlation between Φ at the ice coring sites and large-scale atmospheric circulation.
 1356 Correlations are calculated using annual mean data (all months, April-March). We only list the
 1357 statistically significant correlations ($p < 0.1$). The Niño 3.4 is calculated over 5°S - 5°N, 190°E - 240°E,
 1358 using SST from Huang et al. (2014); the PDO index is from Mantua and Hare (2002).
 1359

Site	SAM	PSA1	PSA2	Niño 3.4	PDO	Sea ice Am-Bell	Sea ice Ross
WDC	-	0.31	-	0.31	0.28	-	-
SDM	-	0.47	0.34	0.43	0.45	-	-0.32
RICE	-	0.41	0.34	0.34	0.45	-	-0.30
SP	-	-	-0.32	-	-0.30	-	-
LD	0.45	-	-	-	-	-	-
DF	0.37	-	-	-	-	-	-
EDC	0.30	-	-	-	-	-	-
JRI	0.67	-	-	-	-	0.31	-
BPBRP	0.68	-	-	-	-	-	-

1360

1361

1362